Status and prospects of X-ray free-electron lasers (X-FELs): a simple presentation

Article *in* Journal of Physics D Applied Physics · May 2012

DOI: 10.1088/0022-3727/45/21/213001

2 authors, including:

G. Margaritondo
École Polytechnique Fédérale de Lausanne
1,059 PUBLICATIONS **17,249** CITATIONS

SEE PROFILE

Status and prospects of x-ray free-electron lasers (X-FELs): a simple presentation

2012 J. Phys. D: Appl. Phys. 45 213001

(http://iopscience.iop.org/0022-3727/45/21/213001)

IOP PUBLISHING JOURNAL OF PHYSICS D: APPLIED PHYSICS

J. Phys. D: Appl. Phys. **45** (2012) 213001 (20pp) doi:10.1088/0022-3727/45/21/213001

TOPICAL REVIEW

Status and prospects of x-ray free-electron lasers (X-FELs): a simple presentation

Primoz Rebernik Ribic and G Margaritondo

Faculté des Sciences de Base, Ecole Polytechnique Fédérale de Lausanne (EPFL), Lausanne, Switzerland

E-mail: primoz.rebernikribic@epfl.ch and giorgio.margaritondo@epfl.ch

Received 8 March 2012, in final form 12 April 2012
Published 10 May 2012
Online at stacks.iop.org/JPhysD/45/213001

Abstract
The first part of this topical review provides the reader with a conceptual background sufficient to understand the mechanism of an X-FEL without using any formalism. The discussion is thus accessible to non-specialized scientists from any discipline. Then, we review the present status of selected X-FEL projects throughout the world. Examples of actual experiments are used to illustrate the potential impact of these new, exciting sources at the forefront of photon technology.

(Some figures may appear in colour only in the online journal)

1. Introduction

The history of optics, imaging and spectroscopy in the 20th century was dominated by the invention of the maser-laser mechanism [1] for microwaves and by its progressive extension to shorter wavelengths [2]. Until very recently, however, no laser was available for short-wavelength x-rays. This is regrettable since the majority of x-ray techniques can strongly profit from the advanced characteristics of a laser source: high intensity and brightness/brilliance, collimation, lateral and longitudinal coherence, monochromaticity and fast time structure. In 2010, the first hard-x-ray FEL started to operate at Stanford [3], inaugurating a series of exciting developments in several countries.

Such developments will have a strong impact on many different disciplines. We thus believe that making them understandable for a broad, non-specialized audience is important, since it enables potential users to become aware of this new opportunity and perhaps to conceive new experiments. This dissemination is the objective of the present review: we will first present the essential mechanism behind X-FELs in extremely simple terms, stressing physics rather than formalism. The presentation is based on our recently developed elementary theoretical description [4, 5] of the FEL mechanism but it eliminates all formal developments to reach an audience as broad as possible. After establishing this conceptual background, we will use it to illustrate the present situation of X-FELs throughout the world, with information on the status of facilities and on some of the first experiments.

2. Semantic accuracy

Before starting our discussion, we will tackle an often-debated issue: is the name 'free-electron laser' justified? The question is legitimate: the term 'laser' refers to optical amplification based on quantum stimulated emission. As we shall see, the X-FEL mechanism is different and based on classical effects [6, 7]. Even the term 'free' is not entirely justified since the emitting electrons are trapped inside the vacuum chamber of an accelerator (and, in a different perspective, an X-FEL is not quite 'free' but rather expensive to build and operate).

Some legitimacy for the name 'free-electron laser' can be provided by the characteristics of the emission [4, 5]—very similar to a real laser—and by the fact that the underlying physical mechanism is optical amplification. Thus, the seemingly unstoppable use of the name 'free-electron laser' can be, if not fully accepted, at least magnanimously tolerated.

3. Building a powerful x-ray emitter: synchrotron radiation

Before the 1960s, the production of x-rays relied on the technology invented by Röntgen [8] in the 19th century: the

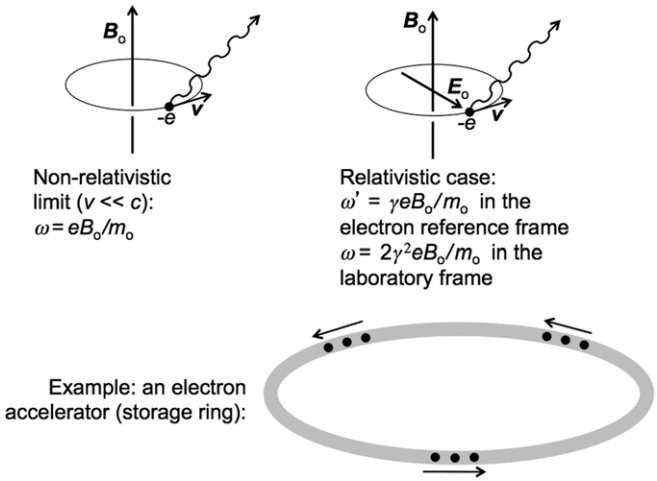

Figure 1. Relativity at work in the case of cyclotron emission by an electron in a B-field. The classical emission frequency $\omega = eB_o/m_o$ changes to $\approx\gamma\omega$ in the electron reference frame and to $\approx 2\gamma^2\omega$ in the laboratory frame.

electron bombardment of a solid electrode. The technology was quite limited as far as brightness, intensity and coherence of the emission were concerned. The late 1960s brought a major revolution with the advent of synchrotron sources [9], in which the emitters are electrons moving in a particle accelerator.

The fact that the magnet system accelerates such electrons forcing them to emit electromagnetic radiation was known from the dawn of accelerator physics. But it was not universally grasped that the relativistic velocity of the particles strongly influences the emission although the theoretical background was already available (an excellent report on the early steps of the field can be found in [10]).

Consider for example (figure 1) the classical (i.e. non-relativistic) frequency of the waves caused by cyclotron motion, $\omega = eB_o/m_o$ (B_o—magnetic field strength; e, m_o—electron charge and mass). This frequency is determined by the Lorentz force of magnitude evB_o. When 'seen' by an electron circulating at a relativistic speed, the Lorentz-transformed B-field also corresponds to an electric field with strength $\approx c\gamma B_o$; the Lorentz force becomes an electrostatic force of magnitude $\approx ec\gamma B_o$. The corresponding cyclotron emission frequency in the electron frame is $\approx\gamma eB_o/m_o$. In the laboratory frame, the (relativistic) Doppler effect further changes this frequency to $\approx 2\gamma^2 eB_o/m_o$.

If $v \ll c$ and the factor $\gamma^2 = (1 - v^2/c^2)^{-1}$ is ≈ 1, the frequency increase by $2\gamma^2$ is not very large. But the contrary is true for an electron accelerator, where $v \approx c$ and the $2\gamma^2$ factor boosts the wave frequency towards the x-ray range.

Relativity also enhances the collimation of the emission. In the reference frame of the electron, the emission occurs in a broad angular range. The Lorentz transformation to the laboratory frame of the transverse photon velocity contains a factor $1/\gamma$, whereas the longitudinal component does not. This 'squeezes' the emission into a narrow cone of width $\approx 1/\gamma$, along the direction of the electron motion.

Therefore, even before the advent of X-FELs, synchrotron x-ray sources emulated [9] many of the laser characteristics such as collimation and the corresponding high lateral coherence. Still missing, however, was a mechanism of optical amplification capable of boosting the emission intensity and brightness: free-electron lasers implemented it [6]. For decades, however, the spectral range of free-electron lasers was confined to long (infrared) wavelengths: the reason will be clarified below.

4. Even more powerful sources

In order to grasp the working mechanism of a free-electron laser [4, 5], consider first the hypothetic x-ray emitter illustrated in figure 2. A bunch of point sources travels at a speed v; when they enter a certain region, they emit waves.

The point sources are not homogeneously distributed in the bunch, but confined to very narrow sheets ('microbunches') perpendicular to the motion. The arrangement is periodic: the distance between two adjacent microbunches equals the emitted wavelength λ. Thus, the waves produced by different microbunches are coherently combined: their field amplitudes, rather than their intensities, add up.

The wave amplitude emitted by a microbunch is proportional to the number of point sources; the total wave amplitude produced by the whole bunch is therefore proportional to N, the total number of point sources in the bunch. The total intensity is proportional to the square of the amplitude and, therefore, proportional to N^2.

How, however, could we construct a nanostructured object like that of figure 2 using electrons as the building blocks? Note that to emit x-rays the microbunch periodicity must be on the Angstrom scale. Luckily, the nanostructured object does not require a sophisticated fabrication technology but is automatically produced in a free-electron laser.

Consider the scheme of figure 3 that illustrates the basic components of a free-electron laser source [4, 5]. A bunch of electrons is accelerated to a speed close to c and then enters an 'emission region' created by a periodic series of alternating magnets (a 'wiggler' or 'undulator', the difference between these two terms not being of immediate concern for our present discussion [9]). The periodic magnetic (B) field forces the electrons to slightly undulate in the transverse direction and the corresponding charge acceleration causes the emission of waves. The relativistic collimation effect discussed above confines this emission to a narrow cone in the longitudinal direction.

The emitted wavelength is linked to the B-field periodicity, but also strongly influenced by relativity [9]. In fact, the magnet period L, when 'seen' by a moving electron, is shrunk by the Lorentz contraction to $\approx L/\gamma$. This is also the emitted wavelength in the electron frame; in the laboratory frame, the Doppler effect further decreases it to $\approx L/(2\gamma^2)$. In this way, relativity transforms a macroscopic magnet periodicity into an Angstrom-size periodicity of x-ray wavelengths; note that the γ^2 factor is the same previously found for the frequency of cyclotron emission.

Before entering the periodic B-field, the electron bunch does not have microbunches. After reaching the B-field region, the first electrons in the bunch start to emit waves. These

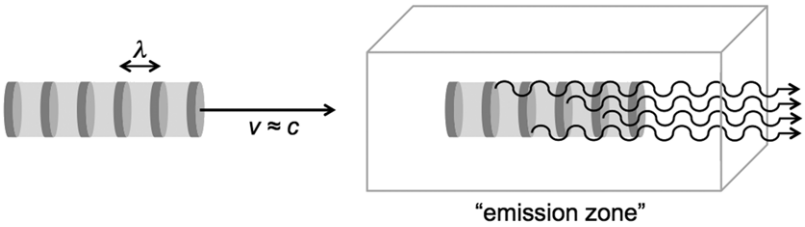

Figure 2. Left: a hypothetic x-ray emitter simulating an X-FEL: a bunch of electrons travelling at a relativistic speed, with a fine structure of periodic microbunches spaced by one wavelength. Right: when the object emits, the waves from different microbunches add up coherently.

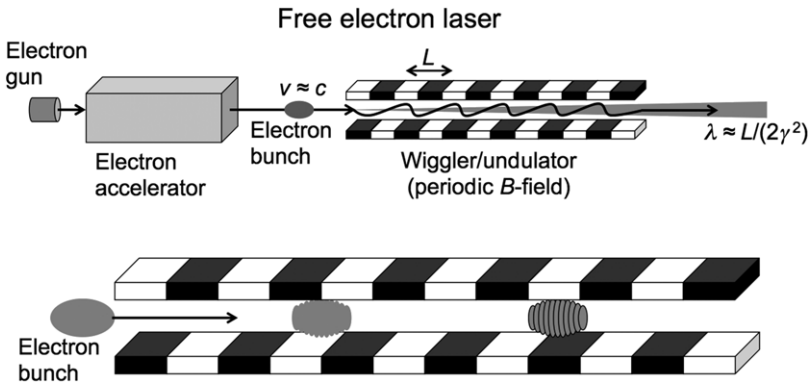

Figure 3. Top: the basic ingredients of a free-electron laser, including an electron gun, an accelerator and an 'undulator' or 'wiggler' that produces a periodic B-field. Bottom: as the electron bunch travels along the undulator or wiggler, microbunches are progressively built. The microbunching is due to the interaction between the travelling electrons and the previously emitted waves.

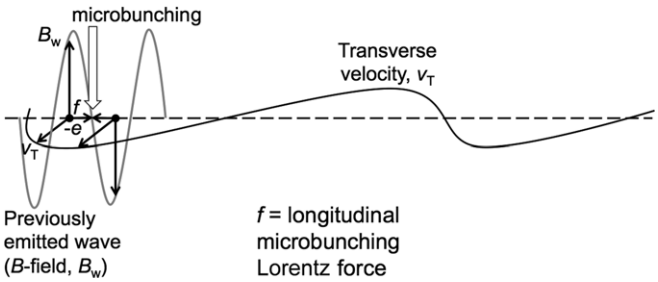

Figure 4. The microbunching mechanism: the transverse magnetic field B_w and the transverse electron velocity v_T cause a *longitudinal* Lorentz force that pushes the electrons towards one of the microbunches. This is true, however, only for waves with the right phase difference between B_w and v_T.

'initial' waves interact with the electrons causing the formation of microbunches—see figure 3, bottom. The unstructured bunch thus evolves into an object similar to that of figure 2, and this starts the optical amplification mechanism.

Figure 4 schematically illustrates how the magnetic field of strength B_w of an 'initial' wave interacts with the transverse oscillations of the electrons [4, 5]. The transverse magnetic field and the transverse electron velocity v_T cause a *longitudinal* Lorentz force that slightly modifies the longitudinal speed of the travelling electrons. If the phase between B_w and v_T is right, the electron is pushed towards a zone of zero B_w. The result is the creation of microbunches with periodicity equal to the wavelength, precisely as in figure 2!

Can this microbunching mechanism, however, be sustained? If the electrons and the wave travelled together

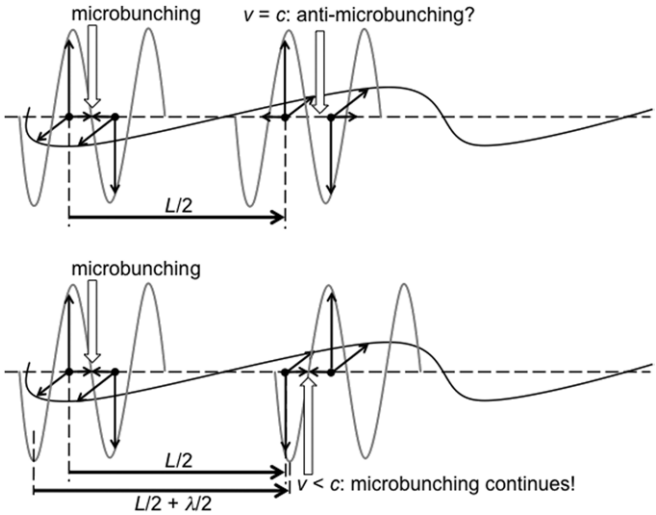

Figure 5. A subtle point: if the electrons and the waves travelled with the same speed (top), after a distance $L/2$ the phase between B_w and v_T would be reversed and the Lorentz force would act against microbunching. But the two speeds are slightly different (bottom) and this allows the continuation of microbunching. In fact, the path difference after the electron travels along $L/2$ is $\approx (c-v)L/(2v) = (c/v)(1-v/c)L/2 \approx (1-v/c)L/2 = (1-v/c)L(1+v/c)/[2(1+v/c)] \approx L/(4\gamma^2) \approx \lambda/2$.

(at the same speed), as illustrated in the top part of figure 5, this would be impossible. After one-half magnet period, the transverse velocity and the Lorentz force would be reversed, acting *against* microbunching. Fortunately, this does not happen: the electron and the wave *do not* travel together, since $v < c$! As seen in the bottom part of figure 5, the small speed

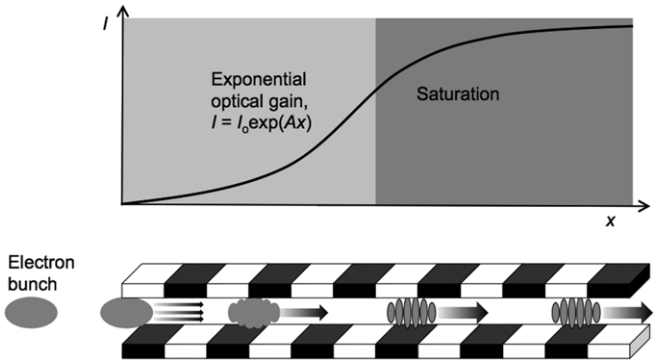

Figure 6. Top: the optical gain causes an exponential increase in the amplified wave until saturation occurs as discussed in the text. Bottom: summary scheme of the X-FEL mechanism—with the initial wave emission, followed by progressive microbunching and amplification of the waves with the right phase, and then by complete microbunching and gain saturation.

difference is precisely what is needed [4, 5] to keep the forces in the direction of microbunching.

4.1. Optical amplification

It is quite easy to understand how the above mechanism can lead to optical amplification. Suppose that at a certain position x the wave intensity is I. The emission of additional intensity by an electron corresponds to transfer of energy from the electron to the wave. This requires a negative work to be done by the wave (transverse) E-field, whose strength E_w is proportional to $I^{1/2}$.

The amount of work done by the E-field on a single electron in a time interval dt is proportional to the product $v_T E_w\, dt$ and therefore to $I^{1/2}\, dt$. Thus, the increase in intensity over a distance dx along the undulator corresponding to a time $dt = dx/v$ due to an individual electron would be proportional to $I^{1/2}\, dx$. But when considering the collective effect of all electrons, we must consider another point: only the waves emitted by electrons in microbunches combine coherently with a strong intensity enhancement.

As the electron bunch travels along the undulator (or wiggler), microbunching progressively increases with the distance x as illustrated in figure 3 (bottom). The effect is proportional [4, 5] to the microbunching longitudinal Lorentz force, which—as we have seen—is proportional to the wave B-field B_w and thus, once again, to $I^{1/2}$.

Therefore, over a distance dx corresponding to a time $dt = dx/v$, the combined effect of progressive microbunching and individual electron emission increases the intensity I by a quantity dI proportional to $I^{1/2} I^{1/2}\, dx$. Thus, $dI = A I\, dx$, where A is a constant. This corresponds to an exponential increase $I = I_0 \exp(Ax)$ (see figure 6, top) and, indeed, to optical amplification [4, 5].

We might ask at this point: why the amplification does not always occur in the undulators and wigglers of all synchrotron sources? To answer, we must realize that the above picture is highly idealized, assuming for example a perfect electron trajectory, a bunch with infinitely small transverse cross-section and perfect periodic magnets. The reality is different: optical amplification requires meeting several exceedingly stringent conditions [6, 7, 9] that make it very difficult to construct a working free-electron laser. Such conditions, as discussed below, are even more stringent for x-rays than for longer wavelengths [7].

4.2. The challenge of building an X-FEL

Because of these difficulties, X-FELs became reality only in the past two years [3, 11, 12] whereas the first infrared free-electron lasers were commissioned several decades earlier [6]. The fact that free-electron lasing is more difficult for x-rays than for infrared radiation might appear counter intuitive at first glance. In fact, building microbunches requires shifting electrons inside the bunch by a distance on the order of a wavelength. Infrared wavelengths are more than four orders of magnitude larger than x-ray wavelengths. Why, then, is shifting electrons by such a large distance much easier than by a fraction of an Ångstrom?

We might be tempted to search the answer not in microbunching but elsewhere. In fact, as for many other types of lasers, the optical gain can be enhanced by an external optical cavity formed by two mirrors that effectively increase the distance over which amplification occurs. Such cavities are used for infrared free-electron lasers—but they do not exist for x-rays, whose normal-incidence reflectivity is extremely low. Even sophisticated techniques such as multilayer coatings fail to produce optical cavities at such low wavelengths.

Therefore, X-FELs must rely on high optical amplification to produce the desired emission without multiple passes. This is certainly a complicating factor with respect to infrared free-electron lasers, but it is not the fundamental reason that makes X-FELs a major technological challenge. The reason must be found in microbunching and more specifically in the role of relativity.

In fact, the microbunching force created by the B_w field and by v_T produces an acceleration—related to the longitudinal shift of the electrons—inversely proportional to the electron mass. Due to the large electron speed, the relevant mass is not the electron rest mass m_o but the much larger relativistic 'longitudinal mass', $\gamma^3 m_o$.

Remember that the emitted wavelength λ is inversely proportional to $2\gamma^2$; therefore the γ-factor is proportional to $\lambda^{-1/2}$, and the electron longitudinal mass to $\lambda^{-3/2}$. Therefore, even if the shifts for microbunching are smaller for x-rays than for infrared radiation, they are still more difficult to achieve because the electrons are much 'heavier'. This made the realization of X-FELs a challenging technological problem whose solution required decades of hard work [3].

4.3. The optical amplification saturates

Since the intensity created by the optical amplification increases exponentially with the distance, X-FELs typically use very long wigglers or undulators. There are limitations, however, in the increase in their length: after a certain distance, the intensity gain saturates [4, 5]—see again figure 6, top.

The theoretical treatment of this phenomenon can be quite complex, but the underlying physics can be understood without

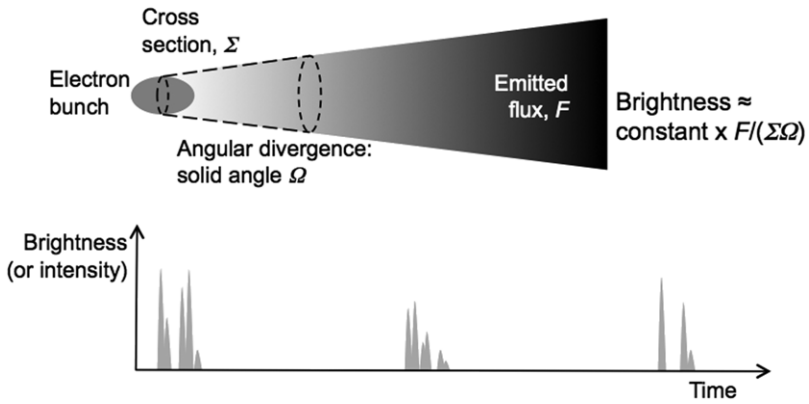

Figure 7. Top: the 'brightness' or 'brilliance', determined by the emitted flux and by the geometry of the emission, characterizes the source quality. Bottom: the time structure of the X-FEL emission consists of very short pulses. The fine structure of each pulse is determined by the random emission of the initial waves, some of which are subsequently amplified.

formalism. As we have seen, optical amplification occurs for 'initial' waves with the right phase, i.e. a phase difference between its E-field and the electron transverse velocity v_T suitable for negative work and therefore for electron → wave energy transfer.

We also discovered that the small speed difference between the wave and the electron is essential to maintain the right phase difference and to guarantee a continuous energy transfer. But we did not yet take into account another important point. As an electron gives energy to the wave, its speed progressively decreases. This means that the speed difference between the electron and the wave progressively deviates from the value needed for continuing electron → wave energy transfer. After a certain distance, the energy transfer is reversed and the wave starts giving back energy to the electrons.

The reversed energy transfer, however, tends to restore the initial phase conditions for electron → wave energy transfer. The system thus oscillates between the electron → wave and wave → electron energy transfer regimes rather than continuing the optical amplification. The optical gain occurs before this oscillation begins, within a distance called 'saturation length', L_S. In essence, a 'good' X-FEL must be designed and realized in such a way that L_S is smaller than the wiggler (or undulator) length [4, 5].

The bottom part of figure 6 schematically summarizes our qualitative findings. Some waves are randomly emitted as the electron bunch enters the undulator (or wiggler). Those with the right phase begin to be amplified due to the combined effects of individual electron emission and progressive microbunching. This causes an exponential increase in the intensity with the distance, until saturation occurs. The increase is characterized by the A-parameter in the $I = I_o \exp(Ax)$ law or by its reciprocal $L_G = 1/A$, the so-called 'gain length'. Shorter L_G values correspond of course to a more effective optical amplification.

What factors influence L_G and therefore the amplification? Once again, qualitative arguments can provide the answer. L_G increases [4, 5] (i.e. the amplification becomes less effective), when the number N of electrons decreases, when the transverse cross-section Σ of the electron bunch increases, when the B-field strength B_o and/or the period L of the wiggler (or undulator) decrease and when γ increases. The qualitative explanations are the following.

The roles of N and Σ are rather obvious: fewer electrons produce less energy transfer, and a larger cross-section decreases the overall intensity and the intensity gain. Likewise, a smaller B_o value means a smaller transverse velocity, a reduced energy transfer and a weaker gain. The roles of the L and γ factors are primarily linked to the above-discussed fact that for small wavelengths the free-electron mechanism is difficult to realize.

With a simple formal treatment, [4] derives the specific dependence of L_G on each of the above factors: L_G = constant $\times (i/\Sigma)^{-1/3} B_o^{-2/3} L^{-1/3} \gamma$. Furthermore, it discusses why the saturation length is proportional to the gain length, the proportionality factor being ≈22.

4.4. The X-FEL output: peak brightness, time structure, coherence

The most important characteristic of the X-FEL emission is a very high peak 'brightness' (or 'brilliance')—see figure 7. The brightness is a merit parameter for wave sources [9], roughly proportional to the emitted flux divided by the source size and by the angular spread of the emission. The emitted flux of an X-FEL is very high for two reasons: first, the emitting electrons are not part of a solid, molecule, liquid or gas but free—they can handle very high-power levels without damaging the host medium. Second, the final flux is boosted by the optical amplification.

The source size is determined by the transverse cross-section Σ of the electron microbunch: the progress in accelerator technology reduced it to very small values [9]. The angular spread is sharply reduced, as we have seen, by the relativistic effect that enhances the collimation. Overall, these factors produce very high brightness.

As shown in figure 7, bottom, the X-FEL emission occurs [4, 5] in short pulses, each corresponding to the passage of an electron bunch through the undulator at a speed ≈c: the bunch length determines the pulse duration. Sophisticated electron beam handling and other measures reduce the pulse duration to the femtosecond scale [3, 11, 12]. This is potentially very

important: such a time-scale is widely believed [13] to be shorter than the time for the explosive propagation of the damage induced by an X-FEL pulse in a macromolecule. Thus, it could be possible to probe the molecular properties before damage occurs, fully exploiting the tremendous peak flux of the X-FEL emission [13].

Coherence—both longitudinal and lateral—is another important characteristic of the X-FEL emission. Lateral coherence [9] is automatically very high. In fact, it increases as the source size and the emission angular spread decrease. Thus, the same mechanisms that enhance the brightness also produce high lateral coherence.

The absolute maximum of the lateral coherence is the Abbe's diffraction limit [14]: the product of source size and angular spread in one direction cannot be lower than, approximately, the wavelength. The X-FELs do reach this limit, and therefore full lateral coherence [3]. The applications of this property are very interesting and very diversified, in particular for different types of x-ray imaging.

The situation is more complicated [4] for longitudinal coherence, which is determined by the emitted wavelength bandwidth. One could hope that a narrow bandwidth gives a high longitudinal coherence. The situation, however, is a bit less favourable.

The wavelength (or frequency) bandwidth corresponds to the Fourier transform of the time structure of the emission. The time structure is determined by the pulse sequence but also by the fine structure of each pulse. Such a fine structure changes from pulse to pulse as shown in figure 7. Each micropulse in the pulse corresponds to an 'initial' wave with the right conditions to be optically amplified. Since the initial emission occurs stochastically, the micropulse timing is random. The corresponding Fourier transform gives a rather broad bandwidth corresponding to limited longitudinal coherence.

How can this problem be corrected? One possibility [4] is not to rely on the random initial emission but to 'seed' the amplification process with a photon pulse produced by another laser. Seeded X-FELs are the subject of intense experimental work throughout the world. Without seeding, the X-FEL mechanism that only relies on the random initial emission is called 'self-amplified spontaneous emission' or SASE [7].

We trust that the above simple presentation provided a sufficient background for discussing actual X-FELs and their applications. Full theoretical approaches can be found in excellent comprehensive publications [15–30] as well as in milestone papers [3, 6, 7] of the free-electron laser and X-FEL history.

5. Review of recent experiments

The most important feature of X-FEL sources that is expected to pave the way to new science is the ability to concentrate vast amounts of energy into a single < 100 femtosecond (fs) pulse resulting in a peak output power of tens of GW, exceeding the one of third-generation light sources by many orders of magnitude. This feature is already being exploited in the state-of-the-art experiments that are being performed at X-FEL facilities and test laboratories around the world.

At present the X-FEL[1] facilities offering beam-time to outside users are LCLS (USA) [3], FLASH (Germany) [31] and FERMI@Elettra (Italy) [32]; for operating parameters see table 1. We will also include the SCSS test accelerator in this review. SCSS is a FEL user facility operating in the extreme ultraviolet regime (EUV); it produces coherent emission in the wavelength range from 51 to 61 nm [33]. Many other X-FELs are either under construction or in their design stage: XFEL in Germany, SwissFEL in Switzerland, PAL-XFEL in Korea, SPARX-FEL in Italy, LCLS-II in USA, FLASH-II in Germany, ARC-EN-CIEL in France, JLAMP in USA, MAX IV in Sweden, POLFEL in Poland, Shanghai FEL in China, TAC SASE FEL in Turkey, etc. For details on the proposed X-FEL projects see table 1. LCLS is currently the only hard x-ray FEL user facility, although lasing at 0.12 nm was recently achieved at SACLA (SPring-8) in Japan and the facility is expected to open its doors to outside users in March 2012.

At present X-FEL facilities already produce radiation down to the Angstrom wavelength range; however, due to limitations of the SASE mechanism and due to a relatively low number of pulses per second that is currently available, the trend is now going towards seeded and high-repetition rate X-FELs, which will offer superior pulse properties and will allow a higher number of experiments to be carried out in parallel.

The following section will give an overview of recent experiments performed at X-FEL user facilities. Since the number of results is rapidly increasing we will not attempt to give a comprehensive review of all the literature that is currently available. Rather than that, we will focus on experiments that have the potential to be implemented as truly novel techniques. In particular, the review will concentrate on multiple ionization of atoms and double-core-hole production with an X-FEL, nanocrystallography and coherent x-ray diffractive imaging and time-resolved imaging and spectroscopy.

5.1. Hollow atoms and double-core-hole spectroscopy

Spectroscopic techniques provide a relatively straightforward way to extract chemical information from the sample under investigation. One powerful spectroscopic method that utilizes x-rays and is often used for chemical analysis is x-ray photoelectron spectroscopy (XPS). XPS is based on photoionization of inner-shell electrons whose binding energies depend on the atom in question (and its environment). During synchrotron XPS the sample is illuminated with a peak power several orders of magnitude lower than that of an X-FEL. The ionization pathways of atoms exposed to intense X-FEL pulses are therefore expected to be substantially different as compared with the case when synchrotron radiation is used. X-FELs thus offer the opportunity to study ionization of atoms under extreme conditions and to exploit the response of matter to intense ultra-short x-ray pulses in order to

[1] We use the term X-FEL to refer to a free-electron laser that can produce coherent emission of x-rays down to a wavelength of ~ 10 nm.

Table 1. Operating X-FEL user facilities and facilities under construction/in their design phase. The list of the latter two may not be exhaustive and the parameters are tentative.

Location	FEL name	Fundamental wavelength range (nm)	Pulse duration (fs)	Maximum no. of pulses per second	FEL Type	Accelerator type	No. of experimental stations/ beamlines	Expected operation
SLAC-SSRL (USA)	LCLS	2.6–0.12	<10–500	120	SASE[a]	Linac[b]	6	Operational
DESY (Germany)	FLASH	44–4.1	10–50	8×10^3	SASE	SC Linac[c]	5	Operational
ELETTRA (Italy)	FERMI@Elettra	100–4	25–200	50	Seeded	Linac	3	Fully commissioned by the end of 2011
SPring-8 (Japan)	SCSS test accelerator	61–51	∼100	60	SASE	Linac	1	Operational
SPring-8 (Japan)	SACLA	down to 0.06	< 100	60	SASE	Linac	currently 2	March 2012
DESY (Germany)	FLASH-II	80–4	10–200	8×10^3	SASE/ Seeded	SC Linac	11	2013
Tor Vergata (Italy)	SPARX-FEL	40–0.6	30–200	100	SASE	Linac	6	2013
PAL (Korea)	PAL-XFEL	5–0.06	<0.5–50	60	SASE	Linac	5	2015
Andrzej Soltan Institute (Poland)	POLFEL	down to 27	10–100	10^5	SASE	SC Linac	∼2	2015
JLab (USA)	JLAMP	100–10	10–100	up to 4.7×10^6	Seeded/ Oscillator	SC Linac	2	2016
SINAP (China)	Shanghai FEL	down to 9 (a hard x-ray FEL also planned)	∼100	50	Seeded (SASE for hard x-ray FEL)	Linac	∼2	2016
Hamburg/ Schenefeld (Germany)	XFEL	6–0.05	<100	2.7×10^4	SASE	SC Linac	10	2016
SLAC-SSRL (USA)	LCLS-II	5–0.1	<10–<100	120	SASE	Linac	10	2018
PSI (Switzerland)	SwissFEL	7–0.1	2–13	100	SASE	Linac	∼6	2019
TAC (Turkey)	TAC SASE FEL	100–1	femtosecond range	5×10^8	SASE	SC Linac	5	2019
SOLEIL (France)	ARC-EN-CIEL	200–0.2	30–300	4.5×10^6	Seeded/ Oscillator	SC Linac	∼4	—
MAX-lab (Sweden)	MAX IV	down to <1	∼100	500	Seeded/ SASE	Linac	∼3	—

[a] Self-amplified spontaneous emission.
[b] Linear accelerator.
[c] Superconducting linear accelerator.

develop new techniques for chemical analysis. The following subsection will provide a short overview of some results of photoionization experiments performed at the new X-FEL facilities. At the end of the subsection we will briefly discuss one potential spectroscopic application.

In the long wavelength regime (optical, near infrared) photoionization of atoms with a laser is a relatively complex process since the photon energy is lower than the ionization energy of the atom. For weak laser electric fields even the removal of a single electron requires multiple photons [34], while for high electric fields the ionization is assisted by tunnelling [35]. Conversely, a single x-ray photon has enough energy to remove an electron from an atom.

When an atom is exposed to x-rays from a synchrotron source it is unlikely that it will absorb more than one photon during a single radiation pulse. In contrast, a focused ultraintense ($\sim 10^{18}$ W cm^{-2}) pulse of an X-FEL will cause an atom to absorb multiple photons [36]. Photoionization experiments at X-FEL facilities were initially performed in the EUV regime [37]. At SCSS in Japan, photoionization of atomic argon was studied using 100 fs FEL pulses at intensities of 2×10^{14} W cm^{-2} and a wavelength of 62 nm, corresponding to photon energies of 20 eV [38]. This energy is higher than the ionization potential of neutral Ar (15.8 eV); consequently the removal of a valence electron can proceed by absorption of a single EUV photon. Although the photon energy was lower

than the ionization potential of Ar^{+} (27.6 eV), charge states up to Ar^{6+} were observed during the experiment. As the ionization energy increases with increasing positive charge on the Ar ion, more than one photon is required to eject an outer electron: for example, the ionization potential of Ar^{3+} is 59.7 eV, therefore three photons with a total energy of 60 eV are needed to reach a higher charge state. Multiple ionization of Ar at 62 nm therefore proceeds by sequential stripping of outer-shell electrons with increasingly more photons required to remove an electron as the positive charge on the Ar ion increases. By studying photoionization of Ar at lower laser intensities ($\sim$5 TW cm^{-2}) it was found that the details of the mechanism are rather complicated and involve intermediate resonances in Ar^{+}, which determine the main ionization pathways and final charge state distributions [39].

At the FLASH FEL multiple photoionization of atomic xenon up to Xe^{21+} during a single laser pulse was observed using a wavelength of 13.3 nm and intensities as high as 10^{16} W cm^{-2} [40]. At this wavelength photons have enough energy to ionize valence as well as shallow-core electrons. Ionization of the latter is accompanied by Auger transitions. The proposed mechanism for the observed multiple photoionization process is sequential single-photon absorption in the initial ionization stage and multiphoton absorption in the later stage when higher ionic species appear [41]. As was the case with ionization of Ar at 62 nm, atomic resonances can complicate the details of this simple description [42].

FLASH pulses were also used to study photoionization of Ar clusters. With illumination intensities up to $\sim 5 \times 10^{13}$ W cm^{-2} and a wavelength of 32.8 nm charge states up to Ar^{4+} were observed [43]. It was found that cluster ionization is a multistep process of direct electron emission events, which are driven by single-photon absorption. At maximum laser power cluster ionization was frustrated due to accumulation of positive charge, which prevented electrons escaping.

At shorter wavelengths ($\sim$1 nm) photons have enough energy to remove deep inner-shell electrons. As opposed to longer wavelengths all of the steps in a multiple ionization process may proceed by single-photon absorption, which makes the photoionization process easier to describe. Recently, photoionization experiments on neon were carried out at the LCLS using three different photon energies: 800 eV, 1050 eV and 2000 eV, corresponding to wavelengths of 1.55 nm, 1.18 nm and 0.62 nm, respectively [44]. By focusing the x-ray beam intensities up to $\sim 10^{18}$ W cm^{-2} were achieved. To determine the charge states of Ne, ion time-of-flight (TOF) mass-to-charge spectroscopy was used. Since the binding energy of a 1s electron in neutral Ne is 870 eV, photons with energy of 800 eV remove only valence (2s and 2p) electrons. The highest charge state of Ne that can be reached at this photon energy is Ne^{8+}. At energies well above the ionization threshold of neutral Ne the cross-section for photoionization of valence electrons drops with increasing photon energy. If the photon energy exceeds the binding energy of the 1s shell, removal of 1s electrons becomes the dominant photoionization process. Therefore, photons having an energy of 1050 eV ionize the 1s shell electrons leaving vacancies behind. Outer-shell electrons rapidly fill these vacancies by Auger decay

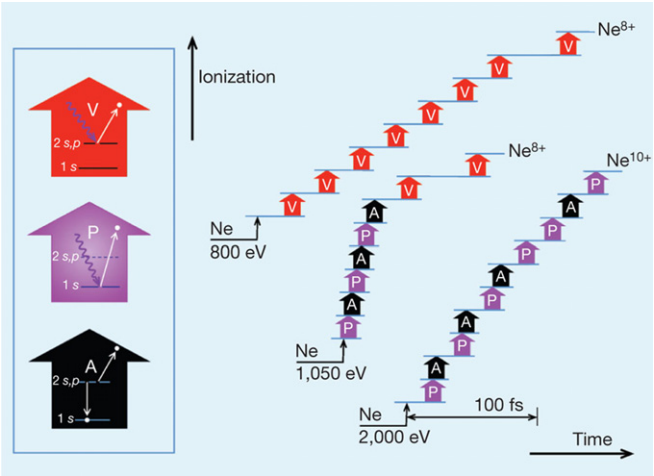

Figure 8. Multiple ionization mechanisms of neon at different photon energies. Below 870 eV x-rays remove outer-shell 2s and 2p electrons (red arrow, V). Above this threshold 1s electrons can be ionized (purple arrow, P). The Auger decay that follows fills the 1s vacancy with an outer-shell electron, which results in another valence electron being ejected (black arrow, A). The processes V, P and A are shown in more detail in the left panel of the figure. Each of these processes increases the charge of the ion by one elementary charge. The right panel illustrates ionization sequences at different photon energies. Reprinted by permission from Macmillan Publishers Ltd: Nature Young L *et al* 2010 *Nature* **466** 56, copyright 2010.

resulting in emission of additional valence electrons. Despite the fact that the photoionization mechanism is different at 1050 eV as compared with the one at 800 eV, photons with energies of 1050 eV cannot remove inner-shell electrons in the positively charged Ne^{6+} or valence electrons of the Ne^{8+} ion and the final charge state that can be reached at a flux of 10^{18} W cm^{-2} is the same in both cases. The reason is that the binding energies of electrons increase with increasing positive charge in Ne. At photon energies of 2000 eV Ne atoms can be fully stripped of their electrons. Detailed schematics of the photoionization process of Ne at different photon energies are illustrated in figure 8.

The above description of photoionization is valid for long laser pulses (>200 fs) where enough time is given for the Auger decay to fill the inner-shells with valence electrons. At photon energies of 2000 eV it was observed that x-ray absorption was significantly decreased for pulses shorter than 80 fs. At this energy x-rays mostly interact with 1s electrons. If these are removed due to an intense ultra-short pulse this will result in decreased x-ray absorption until Auger decay fills the 1s states with valence electrons. The decrease in x-ray absorption is therefore a signature of 'hollow atoms', i.e. due to the short pulse duration the Auger decay cannot replace inner-shell electrons fast enough and therefore the two 1s states remain empty while the outer-shells are still occupied with valence electrons. The presence of these so-called double-core-hole states was also confirmed by electron TOF spectra [44].

Double-core-hole states are not only interesting from the viewpoint of fundamental physics. In molecules double vacancies can be created on a single atom (single-site double-core-holes—ssDCH) or on two different atoms (two-site

double-core-holes—tsDCH). In [45] it was shown, based on calculations performed on C_2H_2, C_2H_4 and C_2H_6, that in the former case the binding energy associated with ssDCH shows relatively low chemical shifts depending on the environment of the atom (site) in question. This is similar to the case in conventional x-ray photoelectron spectroscopy, which is based on single-core-hole ionization. With XPS, difficulties arise when studying molecules containing nearly equivalent atoms, since the binding energies of core electrons are not sensitive to the chemical environment [46]. On the other hand, binding energies of tsDCH show increased chemical shifts depending on the bonding properties of the atoms that carry the holes [45]. Recently, tsDCH were produced in CO molecules using intense x-ray pulses from the LCLS [47]. This may be an important step towards double-core-hole spectroscopy, which could provide important chemical information with enhanced sensitivity.

5.2. Femtosecond x-ray nanocrystallography and coherent x-ray diffraction imaging

For almost a century x-ray crystallography has been the method of choice for obtaining structural information on a wide variety of different materials ranging from inorganic solids and small-molecule organic crystals to biological macromolecules. In order to acquire structural information, crystals of sufficient size have to be grown. In some cases, e.g. membrane proteins, it is very difficult to obtain crystals large enough to record a diffraction pattern with conventional x-ray sources. For small crystals the required x-ray dose for an acceptable signal-to-noise ratio may result in excessive damage to the sample [48, 49]. Even in the case of cryocooled crystals the high x-ray flux may disrupt the structure, which leads to a decrease in diffraction intensity and resolution [48, 50].

There are several processes that can contribute to radiation damage during x-ray exposure. As we have seen in the previous subsection, energetic x-rays may remove electrons from deep inner-shells of the atom. The resulting vacancies are filled with valence electrons by the Auger process, which leads to additional electron emission. The arrangement that is left behind comprises charged atoms close to each other, which may not be stable due to electrostatic repulsion and this eventually leads to the so-called Coulomb explosion. Furthermore, after the ejected electrons leave the atoms they transfer additional energy to the structure by inelastic collisions and may also ionize outer-shell electrons [51]. Another significant effect that also contributes to radiation damage is inelastic scattering of x-rays with the electrons in the atom [50, 52].

Neutze *et al* developed a theoretical model to study radiation damage in protein molecules induced by intense x-ray pulses [52]. They estimated that for short pulses (<10 fs) radiation damage results only in minor displacements of atoms during the pulse, while for longer pulses (∼50 fs) the molecule is destroyed before the pulse is over. The Auger decay in carbon, nitrogen and oxygen atoms takes place on a time-scale of ∼10 fs [53]. Therefore at the end of the laser pulse the number of electrons that escape from the sample and consequently the amount of positive charge that drives the Coulomb explosion is lower in the case of short pulses. Furthermore, an intense ultra-short pulse can produce hollow atoms. The photoionization cross-section for these atoms is reduced and this further limits the number of ejected electrons from the sample. For short pulses the ions do not have enough time to acquire significant kinetic energies by the time the pulse is over and their positions remain virtually unchanged throughout the duration of the pulse. Despite the fact that for both long and short laser pulses the sample is eventually destroyed, it was proposed that the diffraction signal could be collected before the manifestation of the damage in the sample using ultra-short high-intensity pulses from an X-FEL.

The first experimental verification of the above principle was done at the FLASH FEL using intense (4×10^{13} W cm^{-2}) 25 fs pulses at a wavelength of 32 nm to image a pattern on a silicon nitride membrane [54]. The method was recently extended to the hard x-ray regime at the LCLS where diffraction 'snapshots' of the membrane protein 'photosystem I', which is responsible for solar energy conversion during photosynthesis, were recorded at a resolution below 1 nm [55]. Figure 9 shows the experimental setup of the measurement. A liquid jet of protein nanocrystals (sizes ranging from ∼200 nm to 2 μm) with a diameter of 4 μm was introduced into a vacuum chamber where it was intercepted by intense femtosecond x-ray pulses with a repetition rate of 30 Hz and wavelength $\lambda = 0.69$ nm. To reduce the number of situations where more than one nanocrystal was in the focus of a single pulse the concentration of proteins in the liquid jet was diluted to 1 mg ml^{-1}. The diffraction signal was collected on fully hydrated crystals and the setup did not require cryogenic cooling, as is the case in conventional crystallography on microcrystals. To collect the diffraction pattern two CCD detectors were placed at distances of 68 mm and 564 mm from the interaction region of the laser pulse with the liquid jet. The front detector collected scattered x-rays at up to a maximum angle of $2\theta_{\max} = 47.9^\circ$, which, according to the Bragg condition $2d \sin\theta = \lambda$, corresponds to a maximum resolution of $d \approx 0.85$ nm. Small-angle diffraction peaks giving structural information in the range from 100 to 400 nm were recorded with the rear detector.

By focusing the laser beam down to a diameter of ∼10 μm intensities exceeding 10^{16} W cm^{-2} were achieved for 70 fs long pulses. This corresponded to an x-ray dose that is a factor of ∼20 higher than the experimentally determined upper limit of 3×10^7 Gy (1 Gy = 1 J kg^{-1}) for cryocooled crystals [48]. Although the crystals in the laser focus were completely destroyed after a single pulse a diffraction pattern could be recorded before the onset of damage. Because the jet continuously introduced fresh crystals into the laser focus, diffraction patterns could be collected at the repetition rate of the laser (30 Hz).

Diffraction patterns from a single protein nanocrystal recorded on the front detector are shown in figure 10(*a*). At this point it is worth mentioning that in order to collect diffraction snapshots on submicrometre-sized protein crystals, an ultrahigh-power coherent x-ray source is required. Recording diffraction snapshots is therefore possible not

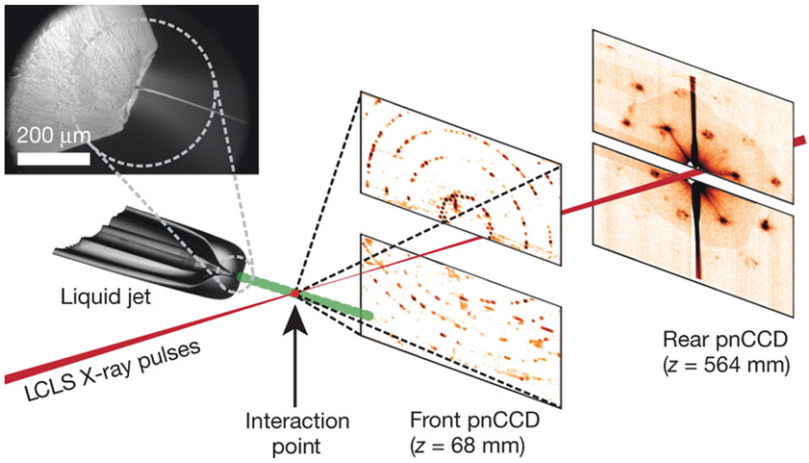

Figure 9. Layout of the diffraction experiment. The X-FEL beam is focused on the liquid jet, which contains fully hydrated crystals. The diffracted x-rays are collected with two CCD detectors. The inset in the upper-left corner shows a scanning electron microscope (SEM) image of the nozzle and the jet. Reprinted by permission from Macmillan Publishers Ltd: Nature, Chapman H N *et al* 2011 *Nature* **470** 73, copyright 2011.

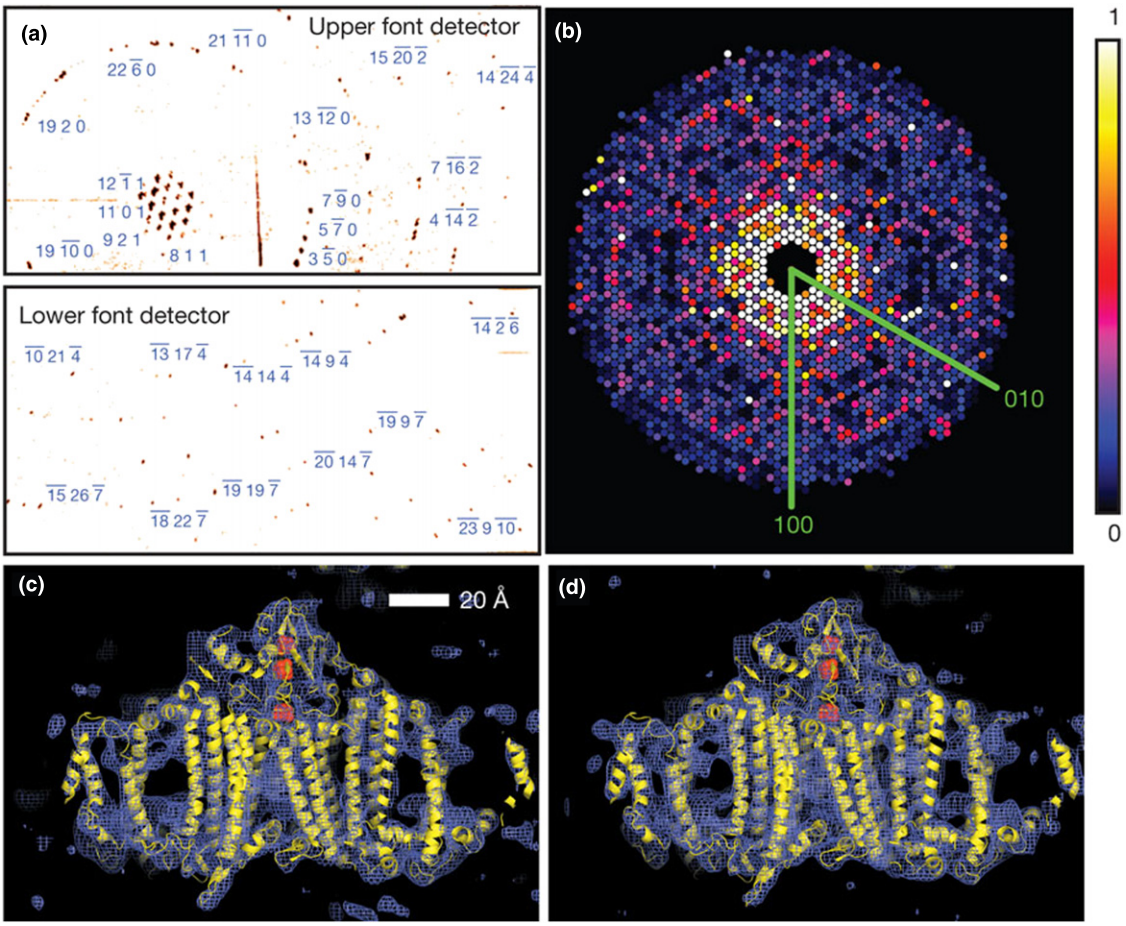

Figure 10. (*a*) Diffraction 'snapshot' of a single nanocrystal of the protein photosystem I. (*b*) Diffraction data from 15000 patterns merged into a single map. (*c*) Electron density map reconstructed from the diffraction map and (*d*) obtained from synchrotron diffraction experiments on photosystem I single crystals (for comparison). Reprinted by permission from Macmillan Publishers Ltd: Nature, Chapman *et al* H N *Nature* **470** 73, copyright 2011.

only due to the ultraintense pulses provided by an X-FEL but also due to the high lateral coherence of the laser. To obtain accurate structural information on the protein, diffraction patterns from more than 15000 crystals had to be merged into a single diffraction map, figure 10(*b*). From the diffraction data the structure shown in figure 10(*c*) was calculated, which was in good agreement with the structure obtained in a conventional synchrotron diffraction experiment

on a cryocooled single crystal of photosystem I, shown in figure 10(*d*) (the high-resolution synchrotron data were truncated at 0.85 nm to enable comparison).

The authors also studied the influence of radiation damage on the diffraction pattern as a function of pulse duration. It was found that the diffraction intensities did not change significantly when going from 10 to 70 fs indicating that radiation damage does not play a crucial role at these time-scales. On the other hand, for pulse durations of 200 fs the intensity was reduced for the high-resolution (beyond 2.5 nm) diffraction peaks, which was a sign of radiation-induced disorder.

Experiments, which aim to increase the resolution down to the atomic scale using shorter wavelengths, are underway (currently the LCLS can produce x-rays with a minimum wavelength of 0.12 nm—the theoretical resolution limit). As noted above, the resolution is also limited by radiation damage, which depends on the pulse duration. To further reduce this effect efforts are planned in order to achieve tighter focusing, thereby increasing the intensity of the x-rays on the sample and allowing the collection of data using even shorter pulses [55]. This would make it possible to collect diffraction data on even smaller crystals with the ultimate goal being able to image a single protein molecule [52].

Although advanced focusing elements based on Fresnel zone plates already show promise in achieving higher intensities [56], at present X-FEL nanocrystallography relies on collection of an ensemble of diffraction patterns, which have to be processed in order to obtain an accurate crystal structure. As already mentioned, many proteins cannot be crystalized into a three-dimensional (3D) structure; however, strategies have been developed to grow 2D and helical crystals using suitable substrates [57–59]. Since the diffraction intensity is proportional to the square of the number of unit cells in the sample, growing large 2D crystals may place less stringent requirements on FEL pulse intensity. Diffraction experiments on 2D protein crystals have been performed using electrons [58]. The disadvantage of this method is that the samples have to be transferred onto a grid and therefore cannot be investigated *in situ*. 2D protein crystallography has also been performed using a synchrotron source; however, due to relatively long exposure times radiation damage may pose a problem in future experiments [60]. In [61] the feasibility of 2D crystallography with an X-FEL was studied at the FLASH FEL using a wavelength of 7.97 nm. An artificial crystal array was prepared on a Si_3N_4 membrane coated with 600 nm of Au and 200 nm of Pd using a focused ion-beam. With a single pulse train, containing a total number of 21 fs pulses, the diffraction pattern of the crystal was successfully recorded and used to reconstruct the 2D image of the sample. Although the resolution of the real-space image was limited to ∼200 nm, this proof of principle may be a significant step towards obtaining the structure of proteins at subnanometre resolutions at the new hard x-ray FEL facilities.

In some cases 2D crystallography may be a viable approach but quite often the structures under investigation are impossible to crystallize. In 1980 Sayre proposed that x-ray diffraction could be extended to image non-crystalline objects [62]. When a periodic object is exposed to x-rays the resulting pattern is composed of well-defined Bragg peaks at angles 2θ with respect to the incoming wave; the peaks satisfy the condition $2d \sin\theta = \lambda$, where d is the distance between crystalline planes and λ is the x-ray wavelength. For a non-crystalline object this is no longer the case but a characteristic diffraction pattern is nevertheless obtained. As in x-ray crystallography the pattern represents the Fourier transform of the object. Since the diffraction pattern only contains information on the scattering amplitude but not the phase, the method suffers from the same 'phase-problem' as encountered in crystallography. The situation is somewhat different for non-periodic objects because the diffraction pattern is continuous rather than being a set of discrete Bragg peaks. This makes it possible to sample the pattern on a much finer scale. This so-called oversampling and iterative phase retrieval algorithms make it possible to reconstruct the real-space image of the object [63, 64]. Although the described method, called coherent x-ray diffraction imaging (CXDI), has to compete with real-space imaging techniques such as x-ray microscopy, the approach does not suffer from resolution limitations imposed by the available optical elements [64].

Femtosecond CXDI was demonstrated at the FLASH FEL on a micrometre-sized non-periodic pattern cut through a 20 nm thick silicon nitride membrane with a focused ion beam [54]. An ultra-intense (4×10^{13} W cm^{-2}), ultrashort (25 fs) FEL pulse with a wavelength of 32 nm destroyed the sample after a speckle-like diffraction pattern was recorded. Using a phase retrieval algorithm [65] the image was reconstructed at the diffraction-limited resolution.

After this successful demonstration of the method in practice, CXDI was extended to image biological samples. It was soon realized that imaging macromolecules attached to semi-transparent silicon nitride membranes with CXDI might pose a problem because the membrane itself scatters x-rays. This scattering may completely overshadow the signal in the case of isolated molecules on a membrane. Therefore the setup was modified in such a way that the FEL beam intercepted particles in free flight (similar to the experiment at the LCLS described earlier, where the FEL beam was focused on the liquid jet containing protein nanocrystals; see figure 9). Using FLASH pulses images of sucrose-encapsulated DNA particles at a resolution better than 40 nm were obtained after reconstructing the diffraction patterns [66].

CXDI was recently implemented at the LCLS, where experiments were performed on single mimivirus (*Acanthamoeba polyphaga* mimivirus) particles [67]. The LCLS was operated at a wavelength of 0.69 nm with pulse durations of 70 fs and peak intensities up to 6.5×10^{15} W cm^{-2}. The experimental setup was similar to the one in figure 9. X-rays scattered from a beam of aerosolized virus particles (diameter ∼0.75 μm) that were injected into the vacuum chamber were collected by a pair of CCD detectors placed at a distance of 564 mm from the interaction region. The upper and lower CCD detectors were separated by a small gap to allow the direct (unscattered) beam to exit. The theoretical resolution limit imposed by the maximum scattering angle was around 10 nm. Figures 11(*a*) and (*b*) show diffraction patterns of two

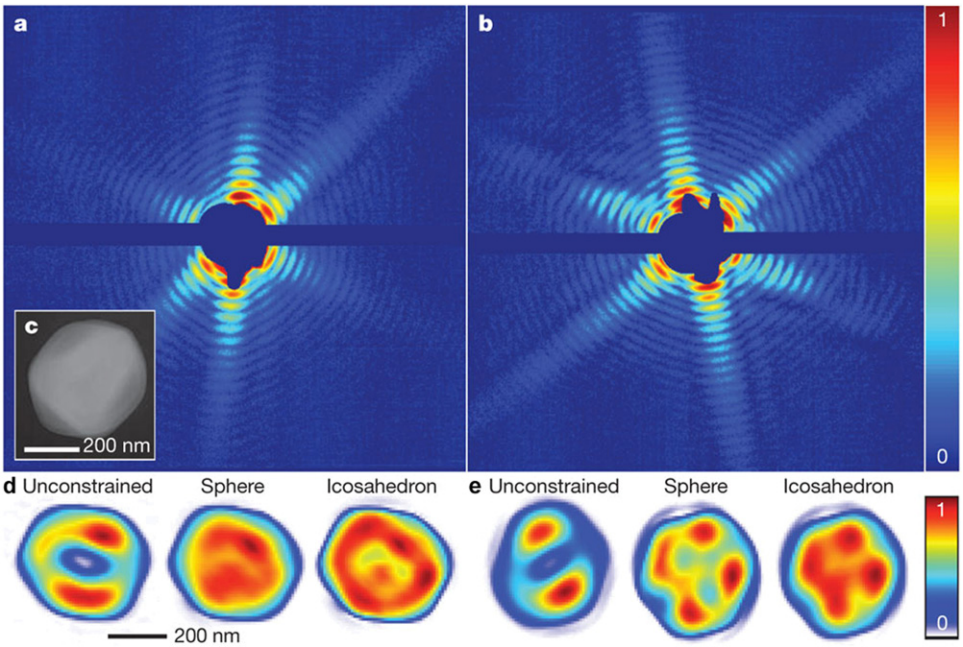

Figure 11. (*a*),(*b*) Single-pulse diffraction patterns of individual virus particles recorded in two different orientations. (*c*) TEM image of the mimivirus particle showing the pseudo-icosahedral shape. (*d*),(*e*) Reconstructed images of the two virus particles from the diffraction patterns in (*a*) and (*b*). Reprinted by permission from Macmillan Publishers Ltd: Nature, Seibert *et al* 2011 M M *Nature* **470** 78, copyright 2011.

mimivirus particles each obtained using a single FEL pulse; the missing low-resolution data are due to the gap between the two CCD detectors. A transmission electron microscope (TEM) image, figure 11(*c*), shows the pseudo-icosahedral shape of the particle. Diffraction patterns were used to obtain the structure of the virus with an iterative phase retrieval algorithm subjected to different geometrical constraints [67], figures 11(*d*) and (*e*). Figures reveal the inhomogeneous interior structure of the virus. The resolution of the real-space images after reconstruction was 32 nm.

The mimivirus was previously studied with cryo-electron microscopy [68]. Although the image resolution was a factor of ∼5 higher, 31 000 images had to be averaged in order to obtain the structure, which illustrates the potential power of single-shot CXDI. In future experiments the resolution is expected to be significantly improved using shorter and more intense laser pulses.

In addition to the obvious advantage of single-shot acquisition of data, there are several other aspects of CXDI that are interesting. In contrast to techniques such as electron microscopy, CXDI can in principle be used to perform measurements on samples in their native environment and does not require special sample preparation such as staining, sectioning and freezing. The low absorption coefficient at x-ray wavelengths also allows imaging of relatively large objects. The technique is currently being tested on a variety of different samples ranging from aerosol particles [69, 70] to single cells [13, 71].

Variations of CXDI have been developed for X-FELs such as in-line-holography (ILH) where a pinhole (placed out of focus of the FEL beam) is used to create a divergent beam that illuminates the sample (in this case the low-resolution data are recovered because there is no need for a gap between the detectors due to a low intensity) or Fourier-transform-holography (FTH) where a pinhole or a reference object is put in the sample plane and imaged along with the sample. Both methods make it easier to retrieve the phase. Coherent x-ray resonant magnetic scattering (XRMS) is another technique that is similar to CXDI except that the x-rays are scattered by magnetic domains instead of electrons. The method gives information on the magnetization density in the sample. For an overview of these methods see, e.g. [71–75] and references therein.

5.3. Time-resolved experiments with x-ray free-electron lasers

Imaging. The power of coherent x-ray diffractive imaging lies in the ultra-short acquisition time required to record a single diffraction pattern. The natural extension of the technique would be to collect a series of diffraction snapshots, i.e. a movie with femtosecond temporal and subnanometre spatial resolution. This would enable to track atomic motion in real-time and make it possible, e.g., to visualize the dynamics of individual biomolecules, observe grain boundary formation in polycrystalline materials, study phase separation and nucleation phenomena, etc.

However, a few obstacles have to be overcome before CXDI can be implemented in time-resolved experiments. In the ultrafast regime the time-evolution of a structure is typically studied using a 'pump–probe' setup, where a pump laser pulse excites the sample and, after a precisely defined time interval, a probe laser is used to record the response. An X-FEL can be either used to probe the sample or provide the excitation pulse or both. The technique relies on precise synchronization between the two pulses. Due to the inherent

statistical nature of a SASE X-FEL the time structure of emitted x-ray pulses fluctuates from one pulse to another. Furthermore, the passage of an electron bunch through a certain point in space can be currently synchronized to ∼100 fs. At present these two factors severely limit the application of X-FEL pump–probe measurements to the femtosecond time-scale. This may change in the near future with the development of seeded X-FELs. Substantial progress in this area has been made at FERMI@Elettra, where coherent emission of x-rays at 65 and 43 nm was achieved using an external seed laser with a wavelength of 260 nm. Experiments are also being performed in order to improve the synchronization accuracy of electron bunch arrivals and to reduce the X-FEL pulse duration, which would further improve the temporal resolution. An alternative approach than can overcome the problem of time-jitter associated with a SASE FEL is to split the x-ray pulse and to use the delayed portion of the pulse as a probe, although this limits experiments to the case where the pump and probe pulses have the same wavelengths. In addition to the above issues there are also CCD detector and data transfer/storage limits that have to be taken into account in the future when high-repetition X-FELs become available. For a comprehensive description of issues related to the implementation of time-resolved imaging with X-FELs, see e.g. [76] and references therein.

Despite the fact that real-space high-resolution imaging methods such as electron microscopy have already been demonstrated on ultra-short time-scales [77], there is increased interest in further development of time-resolved x-ray imaging techniques. As opposed to electrons x-rays have higher penetration depths and do not suffer from resolution limitations imposed by space-charge effects [78]. A much cheaper alternative to an X-FEL is to operate an existing synchrotron as a slicing source [79]. In this approach a femtosecond laser pulse is used to modulate the energy of electrons in a short slice of the electron bunch. The slice can then produce x-ray pulses down to a length of ∼100 fs. The problem is that the peak intensity is much lower than required in order to obtain diffraction images of single particles. Therefore, at the moment, it seems that development of X-FELs with a reproducible pulse time structure is the only viable option if one wants to explore the properties of matter on a femtosecond/subnanometre scale.

In the following we will describe in more detail some of the pioneering time-resolved imaging experiments performed at FLASH. In the paper published by Chapman *et al* [80] the authors studied damage induced by intense FEL pulses in polystyrene nano-spheres. The holographic measurement scheme was inspired by Newton's 'dusty mirror' experiment [81] and is shown in figure 12. Polystyrene spheres (blue) with a diameter of 140 nm were placed onto a 20 nm thick silicon nitride membrane (brown) and illuminated with a focused 25 fs pulse (yellow) with a wavelength of 32.5 nm and a peak intensity ($\sim 10^{14}$ W cm^{-2}) more than 5000 times higher than the damage threshold of polystyrene particles. In this setup the same FEL pulse was used to pump and probe the sample. At time $t = 0$ (figure 12(*a*)) the pulse excited a polystyrene sphere (for clarity the pulse is incident at a small angle). The diffracted x-rays (blue) and the direct beam reached a multilayer-coated mirror (green) placed at a distance l behind the sample at a time $t = l/c$ (figure 12(*b*)). At $t = 2l/c$ the reflected direct beam and diffraction returned to the sample (figure 12(*c*)). By this time the structure of the sphere had changed (indicated by a red ring around the particle) due to the initial excitation by the FEL pulse. Diffraction produced by the reflected beam (delayed diffraction, red) and diffraction from the initial excitation co-propagated (figure 12(*d*)) and interfered at the CCD detector (not shown in figure 12) where information was encoded in the form of a hologram. Due to the high intensity of the FEL pulse both the sample and the mirror were destroyed but not before the interference pattern could be recorded.

Two holograms, both superpositions of time-delayed interference patterns of ∼1000 identical polystyrene spheres, are shown in figures 12(*f*) and (*g*). Due to the high transverse coherence of the FEL beam the individual patterns add coherently resulting in a speckle across the hologram. Both the time-delay between pumping and probing ($2l/c$) and the structural changes are encoded in the hologram. The analysis of the interference pattern is simplified by noting that the problem is equivalent to scattering from two particles separated by a distance $2l$ (figure 12(*e*)). If we consider a detector located at infinity the path difference between the two scattered rays propagating at a small angle θ is $2l(1 - \cos\theta) \approx l\theta^2$. For angles satisfying $l\theta^2 = N\lambda$, where N is an integer and λ is the wavelength the rays add constructively, which explains the fringe pattern observed in the holograms. In case of structural changes of the particle during the time-delay an additional phase shift ϕ is introduced and the optical path difference becomes $l\theta^2 + \phi\lambda/(2\pi)$. By measuring the angles of the bright rings in the holograms the time-delay $2l/c$ could be determined to an accuracy of 1 fs, while the accuracy of the phase shift was 3° for delays less than 1 ps. Using wedge-shaped spacings between the membrane and the mirror and a stair-stepped mirror time-delays between 200 fs and 8 ps were obtained.

The authors observed no changes in the intensity envelope of holograms recorded with a time-delay below 1 ps. For delays longer than 3.8 ps the width of the intensity envelope decreased, which was an indication of particle expansion. This was confirmed by numerical simulations based on the propagation of the FEL pulse through the sphere and subsequent hydrodynamic explosion due to the absorbed energy. The simulations showed a 40% increase in diameter for a time-delay of 3.8 ps. The phase shift proved to be a more sensitive probe for the structural changes. For a time-delay of 350 fs the observed phase shift was 5°, which corresponded to a 6 nm increase in the sphere diameter. Extrapolating these values to the end of the pulse duration gave a maximum expansion of 0.4 nm for the 140 nm sphere. This confirms the results from the previous section, where we have seen that for short FEL pulses CXDI images can be acquired before manifestation of damage.

In the future time-delay x-ray holography could in principle be extended to the hard x-ray regime using grazing-incidence geometry. This would make it possible to track the femtosecond time-evolution of a sample at the subnanometre spatial resolution.

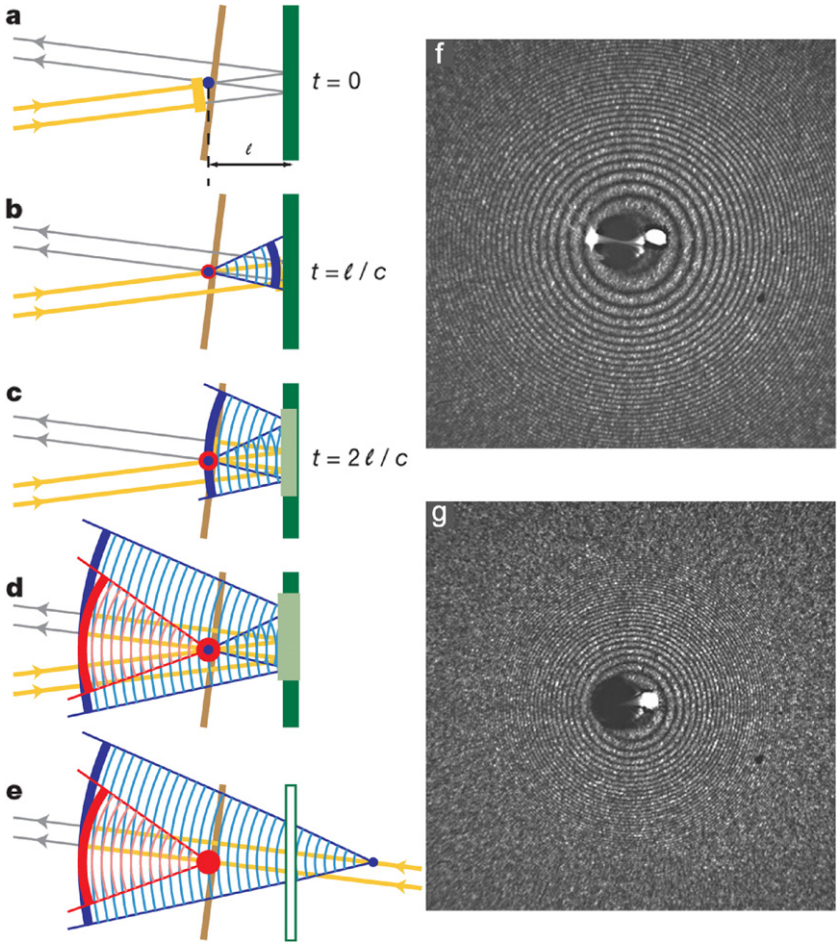

Figure 12. (*a*)–(*e*) Schematics of the femtosecond time-delay x-ray holography experiment (see text for details). X-ray hologram of polystyrene nano-spheres for a time-delay of (*f*) ∼350 fs and (*g*) ∼730 fs. Reprinted by permission from Macmillan Publishers Ltd: Nature, Chapman *et al* H N *Nature* **448** 676, copyright 2007.

One could argue that a more straightforward approach than the one above would be to split the FEL pulse into two beams, introduce a time-delay and an angle between them, and collect the two diffraction patterns with separate CCD detectors. The problem with this method is that, in order to spatially separate the diffraction patterns, a relatively large angle would have to be included between the beams. As a result, two different projections of the sample would be recorded.

Recently, Günther and co-workers used a clever approach to overcome the above issue [82]. They employed FTH to record a two-frame sequence of a nanostructure with a variable delay on the femtosecond time-scale. The setup of the experiment is shown in figure 13. A FEL pulse was guided into an autocorrelator, where it was split into two half beams using a sharp edge of a mirror (i.e. an edge beam splitter). The beams propagated along two separate optical branches with a controllable relative time-delay between ∼25 fs and 20 ps. The two pulses were incident on a NiFe foil that included a test structure (a stylized Brandenburg gate) and 12 strategically placed (pin)holes, which served as reference apertures. In this spatially multiplexed FTH geometry [83] the Fourier transform of a single hologram reconstructs multiple images of the object, as opposed to standard FTH with one pinhole, where reconstruction results in a single image only. Two holograms produced by the two half beams were recorded within the same exposure by a CCD camera.

Figure 14(*a*) shows the illumination geometry (left), the resulting hologram (middle) and the reconstructed image (right) obtained with the two-pulse experiment by introducing a time-delay of 50 fs between pulses and averaging the measurement over 75 two-pulse acquisitions. Each optical arm was used to illuminate the test structure and a set of reference pinholes. Due to the required spatial overlap a small angle was included between the beams. This resulted in a displacement of the centres of holograms by $0.33\,\mu\mathrm{m}^{-1}$, which is clearly seen in the figure. Note that the advantage of this setup is that the angle between the beams is kept as small as possible, avoiding the unwanted spatial and temporal parallax between the images. During reconstruction each pinhole in the test sample generated two twin-images located at $\vec{r}_i$ and $-\vec{r}_i$, where $\vec{r}_i$ was the position vector of the corresponding pinhole, measured with respect to the centre of the test structure. With a suitable choice of vectors $\vec{r}_i$ it was possible to spatially separate reconstructed images obtained by each optical branch. The set of images corresponding to illumination with a particular optical arm could easily be identified by blocking one of the autocorrelator branches during the measurement, as shown

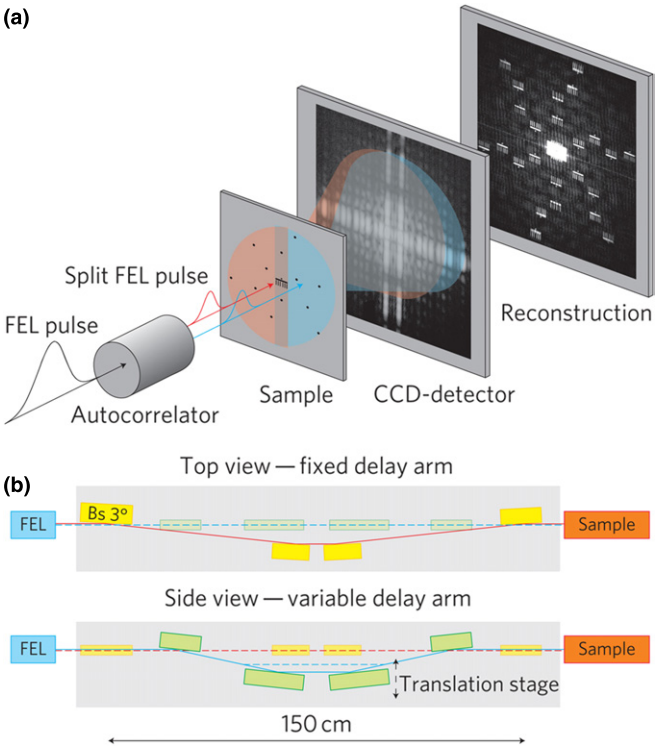

Figure 13. (*a*) Schematics illustrating the FTH setup. The autocorrelator spatially and temporally separates the FEL pulse into two beams. The beams overlap spatially in such a way that they both illuminate the same test structure but different reference apertures. Holograms produced by both beams are recorded with a CCD camera. (*b*) The two optical branches of the autocorrelator. Reprinted by permission from Macmillan Publishers Ltd: Nature Photonics, Günther *et al* 2011 C M *Nature Photon.* **5** 99, copyright 2011.

in figures 14(*b*) and (*c*). It was therefore straightforward to assign the images marked in red in the two-pulse experiment (figure 14(*a*)) as being recorded 50 fs after the images marked in blue. Both the initial and the time-delayed image look the same because the energy density per pulse was below the threshold limit of NiFe (the FEL beam was not focused).

The autocorrelator is capable of producing time-delays below 1 fs, therefore the time resolution of the above method is essentially determined by the duration of the FEL pulse, which is hoped to reach the attosecond time-scale in the future. As opposed to time-delay x-ray holography, the resulting reconstructed images are completely independent. It is expected that the spatial resolution can be further improved by moving to the hard x-ray regime as certain technical issues are overcome [82].

Although the resolution of a 'true' pump–probe experiment with an X-FEL is limited by temporal jitter, picosecond time-scales are still achievable. In a pioneering experiment [84], Barty and others studied the time-evolution of nanofabricated test structures using a pump–probe setup, where an X-FEL pulse was used to probe the sample. Nanometre-size patterns were etched into silicon nitride membranes and illuminated by 12.5 ps pulses from a Nd : YLF laser operated at 523 nm. The peak intensity was large enough ($\sim 2.2 \times 10^{11}$ W cm^{-2}) to initiate sample ablation. The evolution of the sample was tracked by recording x-ray diffraction patterns at different time-delays. Because the initial pulse completely destroyed the sample, several identical copies were needed to produce individual time-delay images. The spatial and temporal resolutions of the experiment were 50 nm and 10 ps, respectively.

Spectroscopy. In addition to the temporal jitter, which is inherent in the current X-FEL pump–probe experiments, partly due to the SASE start up of an X-FEL, SASE is also responsible for the unwanted spectral broadening of the FEL line. As already discussed, the first issue limits the pump–probe experiments mostly to the picosecond time-scales, while the relatively large FEL bandwidth can be reduced by monochromatizing the output beam at the expense of intensity. Although the introduction of a monochromator may reduce the photon flux to that of a synchrotron the advantage of an ultra-short x-ray pulse still remains.

Despite the limitations of SASE X-FELs, recent time-resolved experiments have moved away from pure diffraction imaging to the realm of spectroscopy. In [85] the Verwey transition in magnetite (Fe_3O_4) was observed using time-resolved resonant soft x-ray diffraction (RSXD) with an X-FEL. In this approach the energy of x-ray photons is tuned to match a dipole transition. This provides information about structural as well as electronic properties of a material.

If the temperature of magnetite is decreased below 123 K (the Verwey temperature), the conductivity of the material is lowered by two orders of magnitude through a first-order phase transition, as shown by Verwey in 1939 [86]. During the Verwey transition the lattice undergoes a change from a cubic inverse spinel high-temperature lattice structure to a complex monoclinic low-temperature phase [87]. The transition is accompanied by ordering of the charge fluctuations between octahedrally coordinated Fe^{2+} and Fe^{3+} ions and a spatial modulation of the orbital occupation (see [85] and references therein).

During the RSXD experiment the intensity of a characteristic diffraction peak of the low-temperature phase (0, 0, 1/2) was used as a signature for the transition. When the x-ray photon energy is tuned to the oxygen 1s $\rightarrow$ 2p (K-edge) resonance the (0, 0, 1/2) diffraction peak provides information on the spatial modulation of states at the bottom of the conduction band, which are sensitive to charge/orbital order through O 2p–Fe 3d hybridization. These states are responsible for the energy gap in the low-temperature phase of magnetite. Therefore the resonant (0, 0, 1/2) peak provides direct information on the electronic order as well as the energy position of the involved electronic levels.

A photon energy resolution of $\sim$1 eV was achieved using monochromatized light from the third harmonic of the FLASH FEL to probe the sample. The typical duration of a single FLASH pulse was $\sim$40 fs. Scans across the oxygen 1s $\rightarrow$ 2p resonance were possible due to the relatively large bandwidth ($\sim$5 eV) of the X-FEL. Although the monochromator significantly decreased the intensity, the average photon flux was still comparable to that of a synchrotron. A femtosecond infrared laser (photon energy of 1.5 eV, pulse duration of 130 fs) was used to excite the

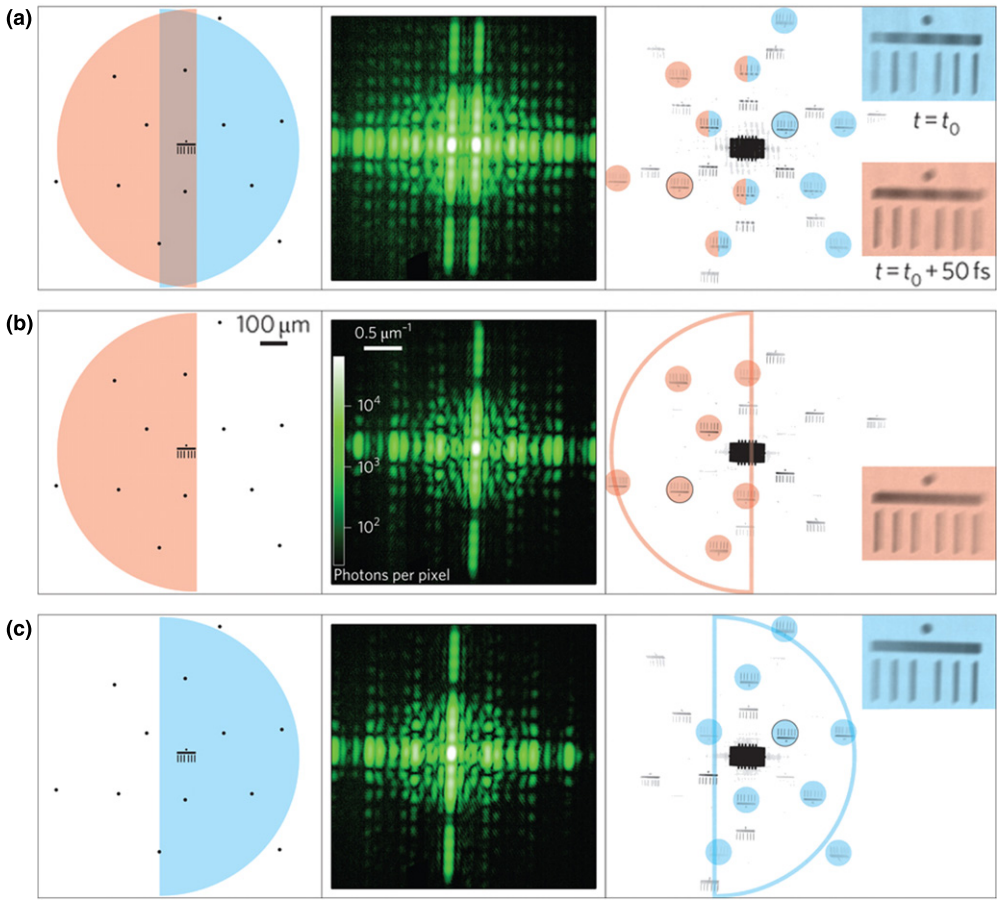

Figure 14. Illumination geometry (left), central part of the hologram (middle) and the reconstructed image (right). The insets in the right panels are magnifications of the images enclosed in black circles. (*a*) Two-pulse experiment with a relative delay of 50 fs. (*b*), (*c*) The same experiment with one of the optical branches of the autocorrelator blocked. Reprinted by permission from Macmillan Publishers Ltd: Nature Photonics, Günther C M *et al* 2011 *Nature Photon.* **5** 99, copyright 2011.

sample. The temporal resolution of the measurement was 210 fs. During the measurements the sample was at 90 K—below the Verwey transition temperature of magnetite.

Figure 15(*a*) shows the intensity of the $(0, 0, 1/2)$ diffraction peak, measured at a photon energy of 529.4 eV, as a function of the time-delay between the pump and probe pulses for different fluences (pulse energies per area). The data clearly show an initial fast decay within the first picosecond followed by a slower decay that persists for several picoseconds. By fitting the data with double exponential decays the time constant of the fast decay was found to be resolution limited (<270 fs) for all fluences, while the time constants for the slower decays were estimated to be tens of picoseconds corresponding to lattice rearrangement. The inset in figure 15(*a*) shows the intensity of the $(0, 0, 1/2)$ peak 200 ps after excitation of the sample measured at BESSY II (a third-generation synchrotron radiation facility). Because the thermalization of the energy deposited by the pump laser should be completed in picoseconds it was surprising that the authors still observed a non-zero $(0, 0, 1/2)$ peak intensity after 200 ps. The estimated temperature in the probed sample resulting from thermalization is shown as the scale in the top axis of the plot in the inset. For all but the lowest fluence the temperature 200 ps after excitation is above the Verwey transition temperature. The authors therefore concluded that the residual peak intensity picoseconds after excitation comes from a transient non-equilibrium phase.

The transient phase was characterized by recording the response of the sample as a function of both time-delay and x-ray photon energy by scanning the monochromator across the X-FEL bandwidth, figure 15(*b*). A ∼0.2 eV shift of the resonance peak to lower photon energies (comparable to the band gap in the low-temperature phase) was observed during transition from the low-temperature to the transient phase. This relatively large energy shift, as compared with the shift previously observed by x-ray absorption spectroscopy (∼40 meV), was a signature of formation of a so far unknown transient phase, characterized by partial charge/orbital order and an almost closed band gap.

Not long ago, the feasibility of time-resolved x-ray photoelectron spectroscopy (TR-XPS) with an X-FEL was proven theoretically and experimentally [88]. The method was recently used to observe a phase transition, similar to the one above, in the Mott insulator $1T$-TaS_2 [89]. It is well established that in $1T$-TaS_2 the interaction of charge and lattice degrees of freedom results in a coupled charge-density-wave (CDW)—periodic lattice distortion (PLD) ground state. Although the quasiparticle and collective dynamics of the CDW-PLD state, the finite electron-lattice coupling time, and the collapse of the

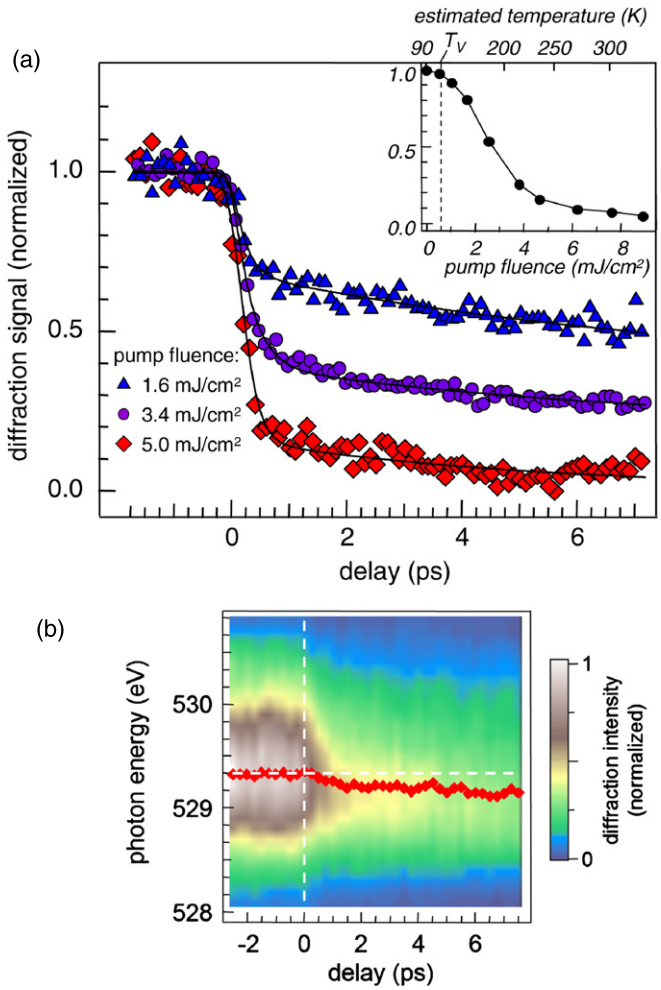

Figure 15. (*a*) Time-resolved oxygen K-edge (0, 0, 1/2) RSXD signal for different excitation pulse fluences. Solid lines are double exponential fits to the data. The inset shows the RSXD signal as a function of fluence 200 ps after excitation measured as BESSY II. (*b*) Oxygen K-edge (0, 0, 1/2) RSXD signal as a function of time-delay and x-ray photon energy. Diamonds indicate the resonant peak position. Reprinted with permission from Pontius N *et al* 2011 *Appl. Phys. Lett.* **98** 182504, Copyright (2011), American Institute of Physics.

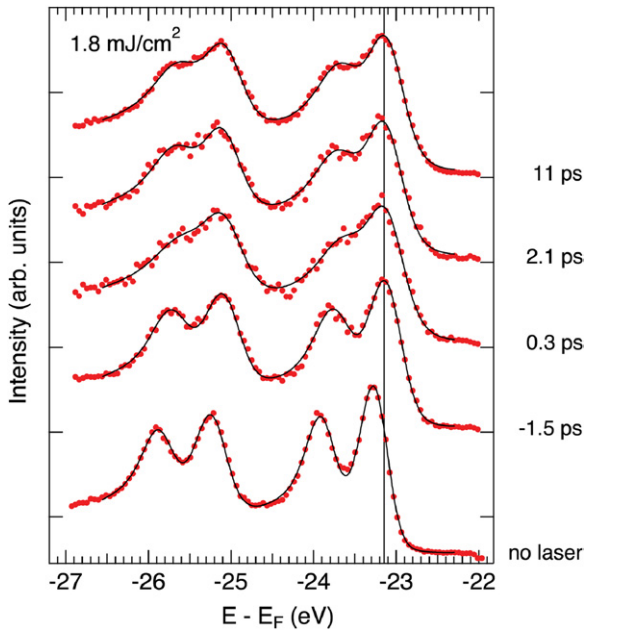

Figure 16. XPS spectra of a $1T$-TaS_2 single crystal as a function of the pump–probe time-delay. Solid lines represent fits to the experimental data (red dots). Reprinted figure with permission from Hellmann S *et al* 2010 *Phys. Rev. Lett.* **105** 187401, Copyright (2010) by the American Physical Society.

band gap under strong excitation are known, it is still unclear how fast a CDW can melt and recondense after excitation.

To study the dynamics of the CDW the transition between a low-temperature (below ∼200 K) commensurate (with respect to the lattice) CDW (CCDW) phase and an intermediate-temperature (∼200 to ∼350 K) nearly commensurate (NCCDW) phase was probed. The Ta $4f$ binding energy was used as a signature for the phase transition. In the CCDW phase each $4f$ level is split into two well-separated peaks and this splitting Δ_{CDW} is a measure of the CDW amplitude. In the NCCDW phase the splitting is less pronounced and reflects the relative size of commensurate domains with respect to discommensurations. Therefore Δ_{CDW} can be regarded as an order parameter of the system.

Single crystals of $1T$-TaS_2 were excited by 120 fs pulses with a photon energy of 1.55 eV and probed by femtosecond FLASH pulses with a photon energy of ∼156 eV (∼8 nm). The energy and time resolutions were 300 meV and 700 fs, respectively. Before excitation with the optical laser the sample was at 10 K, corresponding to the CCDW phase. Two excitation fluences were used: 1.8 mJ cm^{-2} and 2.5 mJ cm^{-2}, both sufficient to heat the excited volume above the CCDW-NCCDW transition temperature. All measured kinetic energies of photoelectrons were referenced to the Fermi energy of the unperturbed system.

Figure 16 shows TR-XPS spectra of a $1T$-TaS_2 single crystal. The two spectral features cantered around −25.5 eV and −23.5 eV correspond to Ta $4f_{5/2}$ and $4f_{7/2}$ core levels, respectively. Each of the levels is split into two peaks separated by Δ_{CDW}. The optical pump laser generates space charge, which results in a shift and broadening of the spectrum (compare the 'no laser' and '−1.5 ps' spectra). The TR-XPS spectra clearly show a reduction in the Δ_{CDW} splitting for both Ta $4f_{5/2}$ and $4f_{7/2}$ levels due to excitation. This reduction takes place on the subpicosecond time-scale. Within a picosecond the system partly recovers into a quasiequilibrium state with a lifetime longer than 10 ps.

By carefully analysing the Δ_{CDW} splitting as a function of time and applying theoretical models the authors concluded that the optical excitation causes a quasi-instantaneous (limited by the time resolution of the experiment) collapse of the charge order by rapidly heating the electrons. The collapse of the CDW is followed by melting of the long-range lattice order of the CCDW phase (with a time constant of ∼900 fs) as the electrons transfer their energy to the lattice. The resulting quasiequilibrium phase is characterized by domain-like short-range charge and lattice order.

TR-XPS was recently employed to study the liquid-liquid phase transition in silicon [90]. In addition to RSXD and TR-XPS other time-resolved spectroscopic techniques are

being tested with X-FELs. One of them is kinetic energy release (KER) spectroscopy, which was recently used to investigate ultrafast extreme ultraviolet induced isomerization of acetylene cations [91].

In the future, improvements in the time and energy resolutions of X-FEL pump–probe spectroscopic techniques will allow us to perform experiments previously not possible due to the power limitations of third-generation x-ray sources. As mentioned in the previous subsection, the temporal jitter associated with the SASE process, which limits the time resolution of pump–probe experiments, will be reduced in a seeded X-FEL. Furthermore, the introduction of seeding will also lead to a much narrower spectral output of an X-FEL. At FERMI@Elettra a high-gain harmonic generation scheme [92] is currently being tested [32]. The input seed is provided by a tunable high-power UV laser with a wavelength range from 190 to 280 nm. In the first undulator (the 'modulator') the UV laser imprints an energy modulation on the electron beam, which is converted into a coherent density modulation with strong harmonic overtones. The magnetic field of the second undulator (the 'radiator') is tuned in such a way that the FEL resonance occurs at a wavelength that is an integral harmonic of the seed wavelength. This results in an output spectral line that is much narrower than in the case of a SASE X-FEL. The spectral bandwidth is further reduced due to an effect called gain narrowing [93]. When fully commissioned FERMI@Elettra is expected to produce almost fully coherent and transform limited radiation. This will lead to new possibilities in the field of time-resolved spectroscopy in the x-ray wavelength regime.

5.4. Last but not least

A number of experiments performed at the new X-FEL user facilities will not be described here in details. These include: desorption [94] and ablation [95] studies on solids, investigations of plasma [96, 97] and cluster nanoplasma formation [98], time-resolved photoelectron imaging [99], near edge x-ray absorption fine structure spectroscopy [100], Thomson scattering [101] and many others. Since the number of published papers is increasing as we speak and due to space limitations we did not attempt to include all of the experimental results that are currently available in this review. The reader is therefore encouraged to visit the websites of X-FEL user facilities for a more comprehensive and updated list of available publications.

6. Conclusion

The goal of the review was to bring the topic of X-FELs closer to a non-specialized audience, i.e. to potential users outside the field of physics. The paper was organized into two parts.

In the first part we introduced the fundamental physics of X-FELs using very simple mathematics. The aim was to explain the mechanism of lasing using free electrons without resorting to complex mathematical models, which we believe are not necessary if one wants to understand only the basic principles behind the process. A number of X-FEL properties were explained without using any equations.

In the second part of the review we focused on some of the groundbreaking experiments performed within the last few years at the X-FEL user facilities. The goal was not to give an exhaustive literature overview but to demonstrate the capabilities and potential of X-FELs. Many of the experiments that were described in detail were proof-of-concept type but nevertheless important demonstrations, which have the potential to open up new opportunities in interdisciplinary science.

The field of X-FELs is rapidly expanding, thus we hope that this review can serve as a reference and encourage specialists from different disciplines to take advantage of these wonderful new facilities.

Acknowledgments

We wish to thank professor Fulvio Parmigiani for helpful discussions on the topic of seeding and for providing up to date details about the ongoing progress at the FERMI@Elettra X-FEL. Our work is supported by the Swiss Fonds National de la Recherche Scientifique and by the Center for Biomedical Imaging (CIBM).

References

[1] Gordon J P, Zeiger H J and Townes C H 1954 Molecular microwave oscillator and new hyperfine structure in the microwave spectrum of NH_3 *Phys. Rev.* **95** 282–4
[2] Schawlow A L and Townes C H 1958 Infrared and optical masers *Phys. Rev.* **112** 1940–9
[3] Emma P *et al* 2010 First lasing and operation of an ångstrom-wavelength free-electron laser *Nature Photon.* **4** 641–7
[4] Margaritondo G and Rebernik Ribic P 2011 A simplified description of X-ray free-electron lasers *J. Synchrotron Radiat.* **18** 101–8
[5] Rebernik Ribic P and Margaritondo G 2012 Physics behind free electron lasers (FELs) based on magnetostatic and optical undulators *Phys. Status Solidi* b at press
[6] Madey J M J 1971 Stimulated emission of bremsstrahlung in a periodic magnetic field *J. Appl. Phys.* **42** 1906–13
[7] Bonifacio R, Pellegrini C and Narducci L M 1984 Collective instabilities and high-gain regime in a free electron laser *Opt. Commun.* **50** 373–8
[8] Roentgen W C 1896 On a new kind of rays *Nature* **53** 274–6
[9] Margaritondo G 1988 *Introduction to Synchrotron Radiation* (New York: Oxford University Press)
Margaritondo G 2002 *Elements of Synchrotron Light for Biology, Chemistry, and Medical Research* (New York: Oxford University Press)
[10] Blewett J P 1998 Synchrotron radiation—early history *J. Synchrotron Radiat.* **5** 135–9
[11] For first operation of the FERMI (Elettra) X-FEL in Trieste, see website http://www.elettra.trieste.it/FERMI/index.php?n=Main.Machine and [32]
[12] Altarelli M 2010 *Magnetism and Synchrotron Radiation* ed E Beaurepaire *et al* (Berlin: Springer)
[13] Seibert M M *et al* 2010 Femtosecond diffractive imaging of biological cells *J. Phys. B: At. Mol. Opt. Phys.* **43** 194015
[14] See, e.g., Born M 1997 *Principles of Optics* (Cambridge: Cambridge University Press)

[15] Brau C A 1990 *Free-electron Lasers* (Oxford: Academic)
[16] Dattoli G and Renieri A 1984 *Laser Handbook* vol 4, ed M L Stich and M S Bass (Amsterdam: North-Holland)
[17] Dattoli G, Renieri A and Torre A 1995 *Lectures in Free-electron Laser Theory and Related Topics* (Singapore: World Scientific)
[18] Feldhaus J, Arthur J and Hastings J B 2005 X-ray free-electron lasers *J. Phys. B: At. Mol. Opt. Phys.* **38** S799–819
[19] Huang Z and Kim K- J 2007 Review of X-ray free-electron laser theory *Phys. Rev. ST Accel. Beams* **10** 034801
[20] Kim K- J 1986 An analysis of self-amplified spontaneous emission *Nucl. Instrum. Methods* A **250** 396–403
[21] Kim K- J and Xie M 1993 Self-amplified spontaneous emission for short wavelength coherent radiation *Nucl. Instrum. Methods* A **331** 359–64
[22] Kondratenko A M and Saldin E L 1980 Generation of coherent radiation by a relativistic electron beam in an ondulator *Part. Accel.* **10** 207–16
[23] Milton S V *et al* 2001 Exponential gain and saturation of a self-amplified spontaneous emission free-electron laser *Science* **292** 2037–41
[24] Murphy J B and Pellegrini C 1985 in *Laser Handbook* ed W B Colson *et al* (Amsterdam: North-Holland)
[25] Patterson B D *et al* 2010 Coherent science at the SwissFEL X-ray laser *New J. Phys.* **12** 035012
[26] Pellegrini C 2000 High power femtosecond pulses from an X-ray SASE-FEL *Nucl. Instrum. Methods* A **445** 124–7
[27] Roberson C W and Sprangle P 1989 A review of free-electron lasers *Phys. Fluids* B **1** 3–42
[28] Saldin E L, Schneidmiller E and Yurkov M 2000 *The Physics of the Free Electron Laser* (Berlin: Springer)
[29] Shintake T *et al* 2003 Status of SPring-8 compact SASE source FEL project *Nucl. Instrum. Methods* A **507** 382–7
[30] Schmueser P, Dohlus M and Rossbach J 2008 *Ultraviolet and Soft-X-ray Free-Electron Lasers* (Berlin: Springer)
[31] Ackermann W *et al* 2007 Operation of a free-electron laser from the extreme ultraviolet to the water window *Nature Photon.* **1** 336–42
[32] Allaria E, Callegari C, Cocco D, Fawley W M, Kiskinova M, Masciovecchio C and Parmigiani F 2010 The FERMI@Elettra free-electron-laser source for coherent X-ray physics: photon properties, beam transport system and applications *New J. Phys.* **12** 075002
[33] Inagaki T *et al* 2008 A compact free-electron laser for generating coherent radiation in the extreme ultraviolet region *Nature Photon.* **2** 555–9
[34] Mainfray G and Manus C 1991 Multiphoton ionization of atoms *Rep. Prog. Phys.* **54** 1333–72
[35] Augst S, Strickland D, Meyerhofer D D, Chin S L and Eberly J H 1989 Tunneling ionization of noble gases in a high-intensity laser field *Phys. Rev. Lett.* **63** 2212–5
[36] Rohringer N and Santra R 2007 X-ray nonlinear optical processes using a self-amplified spontaneous emission free-electron laser *Phys. Rev.* A **76** 033416
[37] Wabnitz H *et al* 2002 Multiple ionization of atom clusters by intense soft X-rays from a free-electron laser *Nature* **420** 482
[38] Motomura K *et al* 2009 Multiple ionization of atomic argon irradiated by EUV free-electron laser pulses at 62 nm: evidence of sequential electron strip *J. Phys. B: At. Mol. Opt. Phys.* **42** 221003
[39] Hikosaka Y *et al* 2010 Multiphoton double ionization of Ar in intense extreme ultraviolet laser fields studied by shot-by-shot photoelectron spectroscopy *Phys. Rev. Lett.* **105** 133001
[40] Sorokin A A, Bobashev S V, Feigl T, Tiedtke K, Wabnitz H and Richter M 2007 Photoelectric effect at ultrahigh intensities *Phys. Rev. Lett.* **99** 213002
[41] Makris M G, Lambropoulos P and Mihelič A 2009 Theory of multiphoton multielectron ionization of xenon under strong 93-eV radiation *Phys. Rev. Lett.* **102** 033002
[42] Richter M, Amusia M Ya, Bobashev S V, Feigl T, Juranić P N, Martins M, Sorokin A A and Tiedtke K 2009 Extreme ultraviolet laser excites atomic giant resonance *Phys. Rev. Lett.* **102** 163002
[43] Bostedt C *et al* 2008 Multistep ionization of argon clusters in intense femtosecond extreme ultraviolet pulses *Phys. Rev. Lett.* **100** 133401
[44] Young L *et al* 2010 Femtosecond electronic response of atoms to ultra-intense X-rays *Nature* **466** 56–61
[45] Cederbaum L S, Tarantelli F, Sgamellotti A and Schirmer J 1986 On double vacancies in the core *J. Chem. Phys.* **85** 6513–23
[46] Siegbahn K *et al* 1969 *ESCA Applied to Free Molecules* (Amsterdam: North-Holland)
[47] Berrah N *et al* 2011 Double-core-hole spectroscopy for chemical analysis with an intense X-ray femtosecond laser *Proc. Natl Acad. Sci. USA* **108** 16912–5
[48] Owen R L, Rudiño-Piñera E and Garman E F 2006 Experimental determination of the radiation dose limit for cryocooled protein crystals *Proc. Natl Acad. Sci. USA* **103** 4912–7
[49] Henderson R 1995 The potential and limitations of neutrons, electrons and X-rays for atomic resolution microscopy of unstained biological molecules *Q. Rev. Biophys.* **28** 171–93
[50] Ravelli R B and Garman E F 2006 Radiation damage in macromolecular cryocrystallography *Curr. Opin. Struct. Biol.* **16** 624–9
[51] Ditmire T 1998 Simulation of exploding clusters ionized by high-intensity femtosecond laser pulses *Phys. Rev.* A **57** R4094–7
[52] Neutze R, Wouts R, van der Spoel D, Weckert E and Hajdu J 2000 Potential for biomolecular imaging with femtosecond X-ray pulses *Nature* **406** 752–7
[53] Krause M O and Oliver J H 1979 Natural width of atomic *K* and *L* level $K\alpha$ X-ray lines and several *KLL* Auger lines *J. Phys. Chem. Ref. Data* **8** 329–38
[54] Chapman H N *et al* 2006 Femtosecond diffractive imaging with a soft-X-ray free-electron laser *Nature Phys.* **2** 839–43
[55] Chapman H N *et al* 2011 Femtosecond X-ray protein nanocrystallography *Nature* **470** 73–8
[56] David C *et al* 2011 Nanofocusing of hard X-ray free electron laser pulses using diamond based Fresnel zone plates *Sci. Rep.* **1** 57
[57] Jap B K, Zulauf M, Scheybani T, Hefti A, Baumeister W, Aebi U and Engel A 1992 2D crystallization: from art to science *Ultramicroscopy* **46** 45–84
[58] Chiu W, Avila-Sakar A J and Schmid M F 1997 Electron crystallography of macromolecular periodic arrays on phospholipid monolayers *Adv. Biophys.* **34** 161–72
[59] Wilson-Kubalek E M, Brown R E, Celia H and Milligan R A 1998 Lipid nanotubes as substrates for helical crystallization of macromolecules *Proc. Natl Acad. Sci. USA* **95** 8040–5
[60] Lenne P- F *et al* 2000 Synchrotron radiation diffraction from two-dimensional protein crystals at the air/water interface *Biophys. J.* **79** 496–500
[61] Mancuso A P *et al* 2009 Coherent-pulse 2D crystallography using a free-electron laser X-ray source *Phys. Rev. Lett.* **102** 035502
[62] Sayre D 1980 *Imaging Processes and Coherence in Physics* ed M Schlenker *et al* (Berlin: Springer) pp 229–35
[63] Miao J, Sayre D and Chapman H N 1998 Phase retrieval from the magnitude of the Fourier transforms of nonperiodic objects *J. Opt. Soc. Am.* A **15** 1662–9
[64] Miao J, Charalambous P, Kirz J and Sayre D 1999 Extending the methodology of X-ray crystallography to allow imaging

of micrometre-sized non-crystalline specimens *Nature* **400** 342–4
[65] Marchesini S, He H, Chapman H N, Hau-Riege S P, Noy A, Howells M R, Weierstall U and Spence J C H 2003 X-ray image reconstruction from a diffraction pattern alone *Phys. Rev.* B **68** 140101(R)
[66] Bogan M J *et al* 2008 Single particle X-ray diffractive imaging *Nano Lett.* **8** 310–6
[67] Seibert M M *et al* 2011 Single mimivirus particles intercepted and imaged with an X-ray laser *Nature* **470** 78–82
[68] Xiao C, Kuznetsov Y G, Sun S, Hafenstein S L, Kostyuchenko V A, Chipman P R, Suzan-Monti M, Raoult D, McPherson A and Rossmann M G 2009 Structural studies of the giant mimivirus *PLoS Biol.* **7** e1000092
[69] Bogan M J, Starodub D, Hampton C Y and Sierra R G 2010 Single-particle coherent diffractive imaging with a soft x-ray free electron laser: towards soot aerosol morphology *J. Phys. B: At. Mol. Opt. Phys.* **43** 194013
[70] Bogan M J *et al* 2010 Aerosol imaging with a soft X-ray free electron laser *Aerosol Sci. Technol.* **44** 1–6
[71] Mancuso A P *et al* 2010 Coherent imaging of biological samples with femtosecond pulses at the free-electron laser FLASH *New J. Phys.* **12** 035003
[72] Spence J C H 2007 Diffractive (lensless) imaging *Science of Microscopy* ed P W Hawkes and J C H Spence (New York: Springer) pp 1196–227
[73] Eisebitt S 2008 X-ray holography: the hole story *Nature Photon.* **2** 529–30
[74] Eisebitt S, Lüning J, Schlotter W F, Lörgen M, Hellwig O, Eberhardt W and Stöhr J 2004 Lensless imaging of magnetic nanostructures by X-ray spectro-holography *Nature* **432** 885–8
[75] Treusch R and Feldhaus J 2010 FLASH: new opportunities for (time-resolved) coherent imaging of nanostructures *New J. Phys.* **12** 035015
[76] Barty A 2010 Time-resolved imaging using X-ray free electron lasers *J. Phys. B: At. Mol. Opt. Phys.* **43** 194014
[77] Lobastov V A, Srinivasan R and Zewail A H 2005 Four-dimensional ultrafast electron microscopy *Proc. Natl Acad. Sci. USA* **102** 7069–73
[78] Armstrong M R *et al* 2007 Practical considerations for high spatial and temporal resolution dynamic transmission electron microscopy *Ultramicroscopy* **107** 356–67
[79] Schoenlein R W, Chattopadhyay S, Chong H H W, Glover T E, Heimann P A, Shank C V, Zholents A A and Zolotorev M S 2000 Generation of femtosecond pulses of synchrotron radiation *Science* **287** 2237–40
[80] Chapman H N *et al* 2007 Femtosecond time-delay X-ray holography *Nature* **448** 676–9
[81] Newton I 1952 *Opticks Book 2* part IV (New York: Dover) (originally published by the Royal Society, London, 1704)
[82] Günther C M *et al* 2011 Sequential femtosecond X-ray imaging *Nature Photon.* **5** 99–102
[83] Schlotter W F *et al* 2006 Multiple reference Fourier transform holography with soft X rays *Appl. Phys. Lett.* **89** 163112
[84] Barty A *et al* 2008 Ultrafast single-shot diffraction imaging of nanoscale dynamics *Nature Photon.* **2** 415–9
[85] Pontius N *et al* 2011 Time-resolved resonant soft X-ray diffraction with free-electron lasers: femtosecond dynamics across the Verwey transition in magnetite *Appl. Phys. Lett.* **98** 182504
[86] Verwey E J W 1939 Electronic conduction of magnetite (Fe_3O_4) and its transition point at low temperatures *Nature* **144** 327–8
[87] Wright J P, Attfield J P and Radaelli P G 2002 Charge ordered structure of magnetite Fe_3O_4 below the Verwey transition *Phys. Rev.* B **66** 214422
[88] Pietzsch A *et al* 2008 Towards time resolved core level photoelectron spectroscopy with femtosecond X-ray free-electron lasers *New J. Phys.* **10** 033004
[89] Hellmann S *et al* 2010 Ultrafast melting of a charge-density wave in the Mott insulator 1*T*-TaS_2 *Phys. Rev. Lett.* **105** 187401
[90] Beye M, Sorgenfrei F, Schlotter W F, Wurth W and Föhlisch A 2010 The liquid-liquid phase transition in silicon revealed by snapshots of valence electrons *Proc. Natl Acad. Sci. USA* **107** 16772–6
[91] Jiang Y H *et al* 2010 Ultrafast extreme ultraviolet induced isomerization of acetylene cations *Phys. Rev. Lett.* **105** 263002
[92] Yu L H 1991 Generation of intense UV radiation by subharmonically seeded single-pass free-electron lasers *Phys. Rev.* A **44** 5178–93
[93] Hotz D F 1965 Gain narrowing in a laser amplifier *Appl. Opt.* **4** 527–30
[94] Siemer B, Olsen T, Hoger T, Rutkowski M, Thewes C, Düsterer S, Schiøtz J and Zacharias H 2010 Desorption of H atoms from graphite (0001) using XUV free electron laser pulses *Chem. Phys. Lett.* **500** 291–4
[95] Stojanovic N *et al* 2006 Ablation of solids using a femtosecond extreme ultraviolet free electron laser *Appl. Phys. Lett.* **89** 241909
[96] Galtier E *et al* 2011 Decay of cystalline order and equilibration during the solid-to-plasma transition induced by 20-fs microfocused 92-eV free-electron-laser pulses *Phys. Rev. Lett.* **106** 164801
[97] Vinko S M *et al* 2010 Electronic structure of an XUV photogenerated solid-density aluminum plasma *Phys. Rev. Lett.* **104** 225001
[98] Saalmann U 2010 Cluster nanoplasmas in strong FLASH pulses: formation, excitation and relaxation *J. Phys. B: At. Mol. Opt. Phys.* **43** 194012
[99] Liu S Y *et al* 2010 Time-resolved photoelectron imaging using a femtosecond UV laser and a VUV free-electron laser *Phys. Rev.* A **81** 031403(R)
[100] Bernstein D P *et al* 2009 Near edge X-ray absorption fine structure spectroscopy with X-ray free-electron lasers *Appl. Phys. Lett.* **95** 134102
[101] Fäustlin R R *et al* 2010 Observation of ultrafast nonequilibrium collective dynamics in warm dense hydrogen *Phys. Rev. Lett.* **104** 125002